How Sn addition influences texture development in single-phase Fe alloys: Correlation between local chemical information, microstructure and recrystallisation

N. Mavrikakis, W. Saikaly, P.R. Calvillo, A.P.C. Campos, S. Jacomet, Nathalie Bozzolo, Dominique Mangelinck, M. Dumont

Correlation between local chemical information, microstructure and recrystallisation: how Sn addition influences texture development in single-phase Fe alloys

N. Mavrikakis[a,b], W. Saikaly[b], P.R. Calvillo [2b], A.P.C. Campos[c], S. Jacomet[d], N. Bozzolo[d], D. Mangelinck[a], M. Dumont [1a,*]

[a]*Aix-Marseille University, Institut Matériaux Microélectronique Nanosciences de Provence-IM2NP, UMR CNRS 7334, France*
[b]*ArcelorMittal Global R&D Gent, Pres. J.F. Kennedylaan 3, BE-9060 Zelzate, Belgium*
[c]*Aix Marseille Université, CNRS, Centrale Marseille, FSCM, CP2M, 13397, Marseille, France*
[d]*Mines ParisTech - PSL University - CEMEF - Centre de Mise en Forme des Matériaux, CNRS UMR 7635 - 1 rue Claude Daunesse, 06904 Sophia Antipolis cedex, France*

Abstract

Sn addition is known to affect the recrystallisation texture development of α-Fe. To date, even though the texture effect of Sn has been experimentally verified, although indirectly, the underlying mechanism has not been studied. In the present study, we focus on the static recrystallisation behaviour of Fe-Si-Sn alloys to elucidate the texture preferences assessing for the effect of Sn solute addition. The experimental approach is based on sequential electron back-scatter diffraction (EBSD) texture analysis complemented with a site-specific chemical analysis of grain boundaries by atom probe tomography (APT). It is directly observed through our experiments that boundary segregation phenomena, which occur at the onset and later stages of recrystallisation, provide crucial understanding of texture development. Especially in the presence of solute, the orientation dependence of the energy stored by deformation largely determines the course of the subsequent recrystallisation. In the Fe-Si-Sn alloy, recrystallisation at the highest stored energy grains is hindered. As a consequence of segregation, $\{001\}\langle 110\rangle$ orientations recrystallise at later stages of the process, forming predominantly grains with orientations of the $\{h11\}\langle 1/h\ 1\ 2\rangle$ fibre. These grains are suggested to form following an oriented nucleation mechanism, while their growth could be interpreted with Ibe and Lücke's theory of selective growth of $26.5°\langle 110\rangle$ boundaries in bcc metals.

Keywords:
recrystallisation, grain boundary segregation, solute addition, texture.

1. Introduction

During the thermomechanical processing of metals desired properties in the final product can be obtained via controlling recrystallisation and the related annealing phenomena [1]. The process of recrystallisation involves the softening of plastically deformed metal by restoring its ductility. Recrystallisation is a structural transformation that progresses heterogeneously and typically its kinetics can be separated in two main stages: nucleation and growth [2].

The term nucleation in recrystallisation typically refers to the incubation and growth stages of a subgrain already present in the deformed microstructure [1]. Considering nucleation, the subgrain model theory was introduced by Cahn [3], Beck [4] and more recently Humphreys [5] in studies that shed light on the nuclei selectivity of recrystallisation. According to these, for a subgrain to become a successful nucleus of recrystallisation, there are two main criteria that must be fulfilled; the nucleus needs to acquire a critical size and a boundary mobility advantage [6]. In some cases the size threshold may be reached during annealing by the process of rotation and coalescence of two or more subgrains as proposed by Hu [7]. Nevertheless, it is also essential to have or to attain a misorientation with its environment to achieve the necessary mobility [6]. Several theories have been developed on the basis of relative grain boundary mobility. Some boundaries with low Σ coincidence site lattice (CSL), are known to have higher mobility than grain boundaries (GBs) with higher Σ or general GBs. Impurities that remain in solid solution are known to drastically alter grain boundary mobility and can impact remarkably grain boundary migration-controlled phenomena, such as recrystallisation and phase transformations [8, 9, 10]. Solute segregation at crystal interfaces largely determines the migration rates of the different boundaries. Aust and Rutter have measured the effect of small addition of Sn on the migration rate in pure Pb and observed that special boundaries are less affected by solute, although overall all boundaries underwent a reduced migration rate [11]. It has been suggested that low Σ GB mobility becomes predominant over the one of general GBs [12], as solute

*Corresponding Author
Email address: myriam.dumont@ensam.eu,+33687980216 (M. Dumont)
[1]currently at: Arts et Métiers Institute of Technology, MSMP, HESAM Université, F-59000 Lille, France
[2]currently at: NLMK Belgium Holdings NV, Rue des Rivaux 2, 7100, La Louvière, Belgium

segregation enhances the mobility contrast in the microstructure [13, 14, 15].

Another important aspect of recrystallisation is the orientation dependence of stored energy [16]. In general by increasing the cold rolling strain in bcc alloys, the orientations present in the cold-rolled microstructure rotate towards the $\{111\}\langle uvw\rangle$, γ-fibre component and $\{hkl\}\langle 110\rangle$ (α-fibre) component. In this case, $\{111\}\langle uvw\rangle$ (γ-fibre grains) are able to accommodate relatively higher amount of strain and have a higher Taylor factor than other grain orientations. As the driving force for recrystallisation is proportional to the stored energy of deformation, parent grain orientations are expected to influence the recrystallisation preferences. An established orientation dependence of the stored energy in subgrain coarsening was shown elaborately by Dillamore [16] and later by Hutchinson [17] in low carbon steels. The study of Hutchinson [17] suggested that nucleation proceeds in an orientation-dependent manner. It has also been shown [18] that nucleation in heavily rolled (75-85%) steels takes place primarily in orientations of high Taylor factor (i.e. high stored energy). In the study of recrystallisation it is therefore essential to evaluate the effect of parent grain structure on the recrystallisation process.

Recrystallisation texture strongly depends on the thermo-mechanical process parameters i.e. annealing conditions and deformation mode, while its formation and orientation dependence to the deformed structure has attracted significant research interest throughout the years [19]. Two major theories have prevailed to explain the origin of the recrystallisation texture: *(i)* by its nucleation preferences; *oriented nucleation*, *(ii)* the observed texture is claimed to be a result of the preferred growth of some grains; *oriented growth*. Nevertheless, to date, both theories are widely used to explain recrystallisation observations and in practice both can contribute to texture formation. As Dillamore and Katoh observed [20], a successful recrystallisation theory must explain both the origin and orientation dependence of the recrystallised grain with the deformed matrix.

In the case of pure Fe and low carbon steels, the recrystallisation texture is typically characterized by a strong $\{111\}\langle 112\rangle$ (component of the γ-fibre) texture with the peak intensity being dependent on the cold rolling reduction [21]. Meanwhile, the $\{411\}\langle 148\rangle$ component is sometimes present in the recrystallisation texture, as it has been reported for interstitial free and electrical steels [22, 23]. The origin of this texture component shares some attention in literature, yet the mechanism of its formation is still under debate, as direct observations are generally lacking. The formation of $\{111\}\langle uvw\rangle$ texture can be influenced by the thermomechanical process parameters and the chemical composition of the alloy [22]. As far as the chemical composition is concerned, the recrystallisation texture can be affected by the presence of elements such as P, Se, Sb, Sn etc. even in low concentrations [24]. In several occasions the intentional addition of solutes is accompanied by a weakening of the γ-fibre [25, 26, 27]. In particular for Sn addition, previous research showed that Sn reduced the $\{111\}\langle uvw\rangle$ texture component intensity, while the intensity of $\{110\}\langle 001\rangle$ increased in the recrystallisation texture [28, 29]. The mechanism via which Sn is thought to affect texture formation is often attributed to the enhanced mobility of some CSL interfaces related to segregation phenomena. However, these texture observations with solute addition were performed in a post-mortem fashion, as samples were characterized at the end of the processing and with no association to Sn segregation state.

Latest technological developments in characterisation methods now allow for the first time to correlate orientation preferences with local chemical composition information. Correlative site-specific characterisation is undoubtedly opening more avenues for deeper understanding in materials science, which means that we have an unprecedented capability of analyzing complex physical mechanisms in recrystallisation texture development. Here, we study the effect of Sn addition on the static recrystallisation of Fe-Si model alloys. Si is a common alloying element in steel and is usually added for the fabrication of core materials in magnetic flux carrying devices [30]. In a previous study, the Sn solute effect on the recovery prior and concurrent to recrystallisation was investigated illustrating the retardation in the softening of Fe-Si-Sn alloys [31]. Nevertheless, the underlying mechanism, with which Sn modifies the crystallographic texture formation during recrystallisation, is not yet fully understood. Materials were studied in the as cold deformed state and as recrystallisation initiated and advanced. A sequential measurement procedure using the EBSD technique was used to monitor the evolution of the microstructure and to assess the role of parent grain orientation in recrystallisation texture development. In parallel, site-specific chemical analysis with atom probe tomography (APT) was performed to measure solute segregation at grain boundaries. Chemical information was used to support the crystallographic orientation observations and to explain the effect of Sn solute addition.

2. Experimental

2.1. Materials

A binary Fe- 3 wt.% Si (Fe- 5.8 at.% Si) and a ternary Fe- 3 wt.% Si- 0.1wt.% Sn (Fe- 5.8 at.% Si- 0.045 at.% Sn) were lab produced with maximum impurity level of 150 ppm. Si is added to stabilize α-Fe and produce a single-phase ferritic alloy in order to study recrystallisation only under the solute effect, both Si and Sn concentrations are within the solid solubility in α-Fe. Therefore, the key factor on recrystallisation development will be solute segregation. The Fe-Si binary alloy provided a reference material to isolate the silicon contribution, assessing merely the Sn effect in the microstructure evolution of iron. Both materials were similarly processed, hot rolled, annealed and then cold rolled at a Von Mises true strain of about $\epsilon = 2$ as described elsewhere [31].

2.2. EBSD measurements

Subsequent static recrystallisation was monitored in a sequential manner with EBSD starting from the as cold deformed state and after fast annealing treatments, following the microstructure evolution in a region of interest (ROI) with a sequence of EBSD scans after each annealing step.

The sequential EBSD experiments were performed in the Centre of Materials Forming (CEMEF), Mines ParisTech, in Sophia Antipolis, using a heating stage that has been developed in CEMEF and set up in a FEI XL30 scanning electron microscope (SEM) equipped with a TSL EBSD acquisition system. Both binary and ternary alloys in the as deformed state, were subjected to an interrupted annealing performed at 700° C within the SEM chamber and characterized by EBSD to monitor the recrystallisation evolution. Fig. 1 displays a typical heat treatment during the sequential EBSD experiment as measured by the thermocouple welded on the sample surface. The heating device has a thin Ta foil on which the sample is point-welded, shown schematically in Fig. 1a. An electrical current goes through the Ta foil so that both the Ta foil and the sample (with dimensions of about $3 \times 4 \times 0.2\,\mathrm{mm}^3$) are heated by Joule effect. This particular experimental setup enables very fast heating and cooling rates up to about $100^\circ\,\mathrm{C\ s}^{-1}$, while temperature is regulated by two thermocouples welded close to the region of analysis. More details on the experimental setup can be found elsewhere [32]. EBSD mappings were performed at room temperature after each annealing cycle, so that the microstructure does not evolve during the acquisition time, which would be a serious drawback for fast-kinetic phenomena. EBSD maps were obtained in a selected region of interest in the initial condition and after each heat treatment cycle. For efficiency purposes, given the repeatability and duration of the experiment, the EBSD mappings were performed with a step size of $2\,\mu$m to be completed within less than 60 minutes covering an area of $400\,\mu\mathrm{m} \times 600\,\mu$m. Additional EBSD measurements were performed on the initial state of the materials using a Zeiss Gemini 500 field-emission gun scanning electron microscope (FEG-SEM) equipped with an EDAX Hikari Super acquisition system. These EBSD scans were performed using a finer step size down to $0.05\,\mu$m. Crystal orientations throughout this manuscript are expressed using the conventional orientation representation shown as Orientation Distribution Functions (ODFs) within the Euler space (ϕ_1, Φ, ϕ_2 = 0-90°, due to the orthorhombic sample-crystal symmetry of the bcc structure) and their intensity is expressed in multiple random density [33].

2.3. Heat-treatment in SEM chamber

Starting from the as deformed state, samples were heat treated inside the SEM on the heating stage. The heat treatment applied to both binary and ternary was similar, but longer accumulative holding time was used in the case of the ternary due to slower recrystallisation kinetics [34]. During the 1st heating step, a heating rate of $35^\circ\,\mathrm{C/s}$ was followed, while the following heating steps were performed with the maximum possible heating rate $\sim 100^\circ\,\mathrm{C/s}$. Short isothermal holdings at 700° C were applied and holding time was gradually increased once the kinetics became slower, i.e. during the second half of the transformation, and until almost full recrystallisation was achieved. To analyse the kinetics of recrystallisation, the non-isothermal heat-treatments followed in this study (including heating/cooling sections) Fig. 1b, needed to be converted into isothermal. For this purpose, the approach of Whittaker and Sellars was used to convert the heating time into an equivalent isothermal time [35].

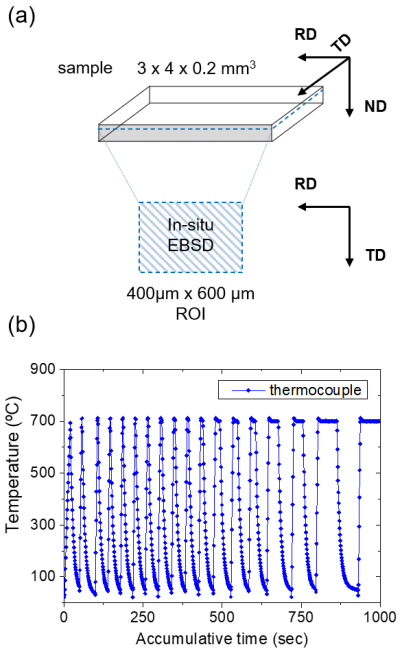

Figure 1: a) Sample configuration tested with EBSD and b) heat-treatment scheme followed during the sequential EBSD experiment in the SEM.

2.4. Data treatment

All EBSD data post-processing was performed with the OIM Analysis platform. The low-to-high angle boundary transition was set at 15° [36], hence low-angle boundaries (LAGBs) were defined for $2^\circ \leq \theta \leq 15^\circ$ and high-angle boundaries (HAGBs) for $\theta \geq 15^\circ$. Recrystallised grains were defined as grains bounded by HAGBs and by imposing the following additional misorientation criteria; a recrystallised grain must have a low internal average misorientation (GOS $\leq 1.8^\circ$). The areas that did not fulfill the aforementioned criteria, were considered as non-recrystallised (non-RX) or recovering microstructure and mainly consisted of a subgrain structure (minimum angle for subgrain definition, $\theta_c \geq 2^\circ$). To include all newly formed grains, after a thermal treatment, a grain definition at the subgrain level was necessary 5° and a more relaxed orientation spread threshold of$\leq 2.5^\circ$; such data segmentation will be referred to as all new grains. In other words, these grains are products of both recovery and recrystallisation excluding the not recrystallised regions of the microstructure.

Besides the recrystallisation state, further analysis of the EBSD data was conducted by segmenting the microstructure also as a function of parent grain orientation, i.e. as deformed prior grains. For this purpose, the image quality (IQ), orientation information from the IPF maps and prior grain boundary locations were combined. In the as deformed state (Fig. 2 and Fig. 4 initial), bright and dark regions represent high IQ corresponding to low stored energy (LSE) regions and low IQ corresponding to high stored energy (HSE) regions, respectively.

For simplicity, in the present study we consider the as deformed state to be binary consisting of HSE and LSE regions only. HSE regions include the main components of the γ-fibre $\{111\}\langle 110\rangle$, $\{111\}\langle 112\rangle$ and the higher dislocation density components at $\Phi > 35°$of the α-fibre. LSE regions include the orientations of the α-fibre centered at the $\{001\}\langle 110\rangle$ component and its vicinity (at $\Phi = 0°$). LSE also include the $\{112\}\langle 110\rangle$ of the α-fibre [37] as this orientation is also known to recrystallise at a later stage of static recrystallisation. The reader is referred to the Supplementary Material for more details on the data segmentation.

2.5. Atom probe characterisation

From the EBSD scanned areas, regions of interest were selected and prepared into tips for APT. Site-specific sample preparation was performed in a FEI Helios NanoLab 600 Dual Beam focused ion beam (FIB – SEM), following the lift-out technique as described elsewhere [38]. Atom probe experiments were conducted in a LEAP 3000XHR instrument with a detector efficiency of 0.37. All measurements were performed in voltage mode, with the sample base temperature and the pulse fraction set at 70 K and 20%, respectively. The APT data were analysed with the IVAS software after calibration of the reconstruction parameters [39]. Finally, segregation at the interfaces was quantified using the well-established method of the Gibbsian excess number, Γ_i^{GB} [40]. Such analysis yields a value of concentration insensitive to the measurement resolution and inclination angle of the interface with respect to the axis of analysis [41].

3. Results

3.1. The as deformed state

In our previous study, the deformed state ($\epsilon = 2$), at the RD-ND plane, was analysed in-depth using EBSD measurements and performing a dislocation density calculation based on misorientation data [31]. Overall, the analysis of the deformed state, on the basis of deformation features, fraction of main texture components and stored energy analysis from EBSD [31], suggested that the addition of Sn neither induced noticeable solid solution strengthening nor alter the known stored energy sequence (in agreement with the work of Dillamore et al. [16]) and that the binary and ternary alloys have very similar as deformed microstructures at this stage. Although in the annealed state prior to cold rolling, the ternary alloy had a finer microstructure as a result of Sn addition, the grain sizes after intermediate annealing were 145 and 104 μm for binary and ternary alloys, respectively.

The regions of interest investigated during the experiment were chosen to be as representative as possible of the overall as deformed state. In the initial scans, as deformed $\{111\}\langle uvw\rangle$ as well as $\{001\}\langle 110\rangle$ oriented grains were included in the area of analysis. Their respective volume fraction in the as deformed state, may not represent accurately the global one but the focus is to study their behavior and interaction during recrystallisation. In both materials large non-indexed areas are also included in the EBSD maps (black zones in Fig. 4). Fig. 2 shows a high resolution EBSD overview of the as deformed microstructure

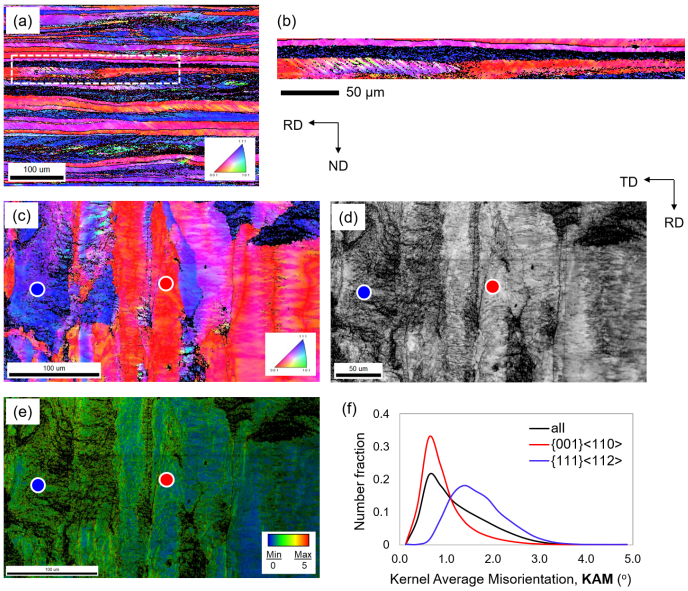

Figure 2: An overview of the as deformed (initial) microstructure in the ternary alloy measured by EBSD. a-b) in the ND-RD section: the ND-IPF map a)through the entire sample thickness and b) at a ROI between different prior grain orientations. c-f) in RD-TD section, at a similar position in the ND axis as in the sequential experiment: c) the ND-IPF mapping, d) the IQ image, e) the 1st neighbor KAM mapping and f) the average KAM measured in the high stored energy (HSE) and the low stored energy (LSE) regions.

in RD-TD section, acquired at a similar position in the ND axis as the one in the sequential EBSD experiment. It can be seen that non-indexation can be correlated to higher amount of local dislocation density and is orientation dependant. For example, the kernel average misorientation (KAM) of the as deformed $\{111\}\langle 112\rangle$ orientation is seen to be more than double that of the $\{001\}\langle 110\rangle$ orientation (Fig. 2e-f). Hence, it is suggested that these highly deformed, non-indexed regions within the area of analysis in Fig. 4 have a near $\{111\}\langle uvw\rangle$ orientation, something that is also confirmed by their neighboring indexed orientations.

3.2. Global recrystallisation behaviour

The global recrystallisation behaviour in the two alloys, Fe-Si (binary) and Fe-Si-Sn (ternary) has been reported in detail in a previous work [42] (see Supplementary Material). That study focused on the effect of Sn addition on recrystallisation texture analysing several thousands of grains by EBSD. Furthermore, the recrystallisation kinetics in the two alloys was quantified by interrupted dilatometer heat treatments and optical image analysis. Fig. 3 shows the overview of the recrystallisation texture for similar recrystallisation fractions ($X_V = 0.2, 0.5, 0.8$) in the two alloys. It was observed that Sn resulted in a softening of the recrystallisation texture by reducing the intensity of $\{111\}\langle 112\rangle$ - from x12.9 mrd to x4.0 mrd at $X_V = 0.2$ (Fig. 3a-b). Whereas the peak intensity in the ternary microstructure was the Goss – $\{110\}\langle 001\rangle$ component, which suggested that shear band nucleation of recrystallisation is less (if at all) affected by Sn. Both the EBSD data and recrystallisation kinetics suggested that the most significant effect of Sn was during nucleation and early

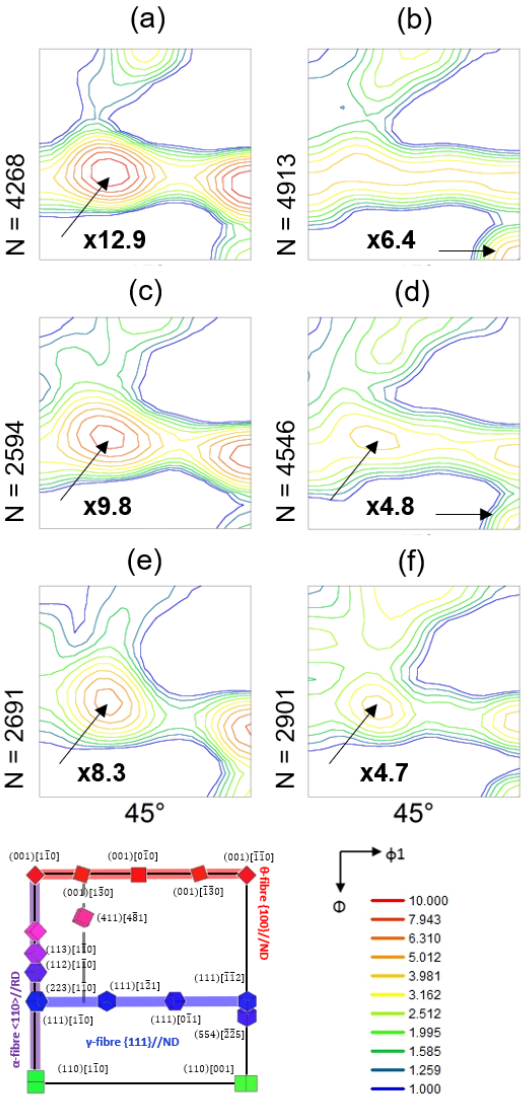

Figure 3: Micro-texture ODFs at the ϕ_2 = 45°section of the Euler space showing the evolution of recrystallisation texture at 700° C from large-scale ex situ EBSD measurements for (a,c,e) binary and (b,d,f) ternary alloy at 0.2 - 0.5 - 0.8 fractions recrystallised, respectively. The max. intensities and numbers of RX grains included are given for each ODF plot (more details are provided elsewhere [42]).

stages of recrystallisation [42]. At later stages of recrystallisation, these observations remained and in the case of the ternary alloy other orientations emerged in the recrystallisation texture (Fig. 3d and f). This behaviour will be discussed in detail in the following sections, in view of local, sequential, EBSD measurements and chemical analysis with APT.

3.3. Sequential observation of recrystallisation

EBSD analysis after sequential annealing at 700°was performed to evaluate the evolution of the microstructure during recrystallisation in the two alloys and the role of the parent grain orientation. Fig. 4 shows the ND- inverse pole figure (IPF) maps as recrystallisation progresses in the two alloys. The IPF maps reveal a clearly different recrystallisation behaviour for the two alloys. The binary alloy was observed to recrystallise rapidly, with small recrystallised grains appearing already after the first heating step (without soaking at 700° C, t = 0s). Moreover, recrystallisation was nearly completed after only 10 seconds of accumulative soaking time. On the other hand, the ternary alloy exhibits much slower recrystallisation kinetics, suggesting that Sn retards the onset of recrystallisation. Indeed, first recrystallised grains were observed after more than 10s accumulative time and more than 2000s accumulative time was necessary to complete recrystallisation within the analysed region. Nevertheless, in both alloys recrystallisation initiates in the γ-fibre parent grains (blue / non-indexed areas in Fig. 4), as expected from stored energy considerations.

Fig. 5 shows the evolution in normalised surface area of the main annealing texture components of all the new grains in the two alloys – as recrystallisation initiates and advances to almost completion (i.e. relative recrystallisation fraction, X_V^{rel} = 0.84 – 0.93). In the recrystallisation texture of the binary alloy, the {111}⟨112⟩ component appears early in the process and becomes dominant at the later stages of recrystallisation. The {111}⟨112⟩ component grows to almost twice the area fraction of the other orientations, and a substantial growth occurs at about X_V^{rel} = 0.7. The texture evolution for the ternary alloy (Fig. 5b), shows in contrast to the binary microstructure, that the {111}⟨112⟩ component stays at rather low values of area fraction during recrystallisation. Moreover, an increase of the {100}⟨120⟩, {411}⟨148⟩ and {111}⟨110⟩ orientations is observed. These observations relate to the parent grain orientations and stage of recrystallisation, and this will be further discussed in the following sections. The experiment shows that the parent grain orientation plays a crucial role in the recrystallisation sequence, while their kinetics is quite diverse. Hence, a segmentation of the microstructure as a function of parent grain orientation is relevant. The length scale and orientation data of the sequential EBSD experiment permit to analyse the recrystallisation kinetics at the parent grain scale and this subject will be considered in the following sections.

3.3.1. Recrystallisation as a function of parent grain

The segmentation of the as deformed microstructure as a function of stored energy enables the evaluation of the individual kinetics within either the HSE or the LSE regions of the

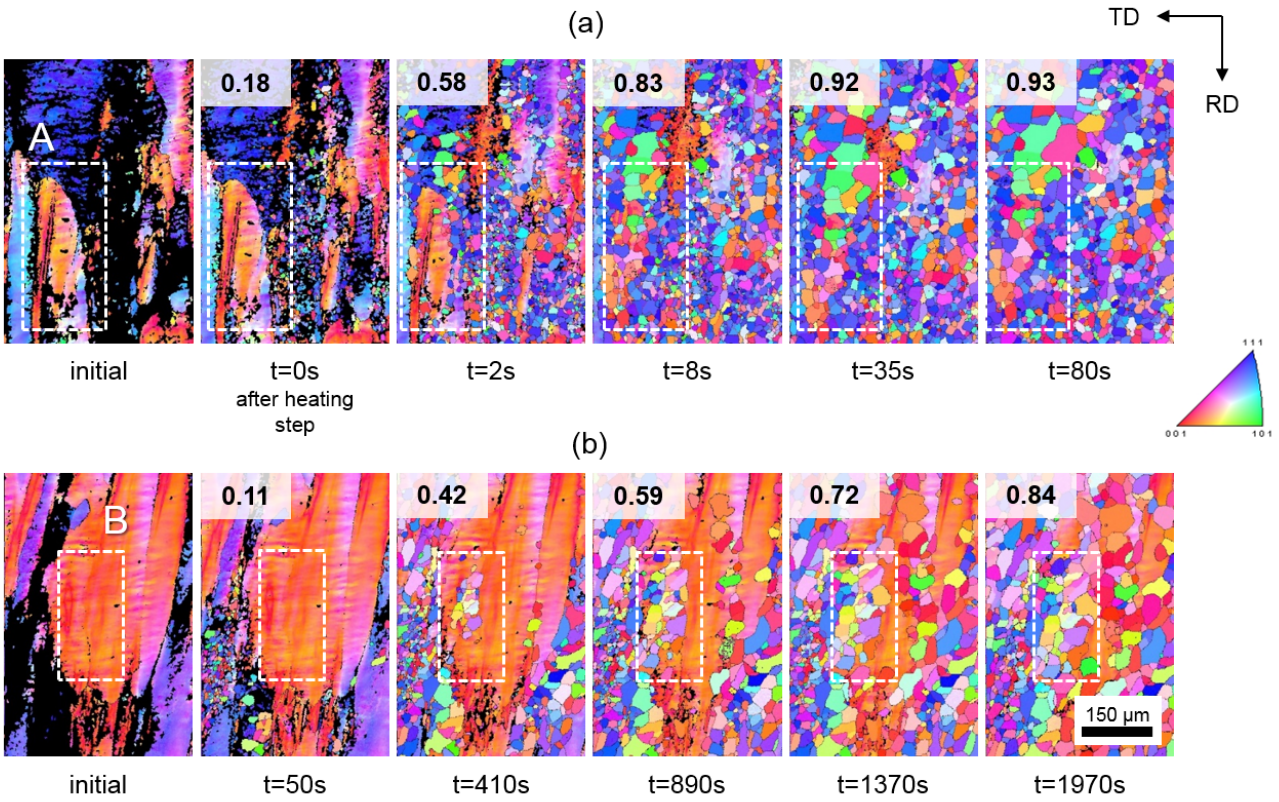

Figure 4: Sequential EBSD ND-IPF + GBs mappings of recrystallisation during annealing in a) binary and b) ternary alloy. The relative recrystallisation fractions are given at each step, lines represent GB misorientations of 8 – 65°.

microstructure using the Johnson–Mehl–Avrami–Kolmogorov (JMAK) analysis [43]. Fig. 6 shows the individual recrystallisation kinetics in the HSE and LSE regions for the binary (Fig. 6a) and for the ternary alloy (Fig. 6b), respectively. The parameters of the JMAK model fitted to the EBSD data are listed in Table 1. The overall JMAK exponent in the kinetic law for the binary alloy is close to unity. For the ternary alloy, the JMAK exponent is different depending on the prior grain stored energy. HSE regions were found to recrystallise with an exponent n of about 0.6, while the LSE regions recrystallise later but much faster, n = 1.2.

Table 1: The JMAK kinetic model parameters from EBSD. The parameters of the recrystallisation kinetics are only given for fractions $0.1 < X_V < 0.9$ [44]. The t_{50} [1] is given in seconds.

		Overall	HSE	LSE
Binary	n	1.0	–	
	t_{50}	2.4		
Ternary	n	0.7	0.6	1.2
	t_{50}	565	81	1080

Fig. 7a shows the growth rates of recrystallised grains within each region. Black arrows in Fig. 7a designate the moment when recrystallisation proceeds in the LSE regions. The binary alloy recrystallises rapidly and the recrystallised grains grow fast. Overall the kinetics cannot be separated since HSE regions recrystallise and migrate into the LSE regions. Hence, the kinetics of the binary alloy represents that of recrystallised grains from the HSE regions. On the contrary, the ternary alloy recrystallises in a more individual manner; HSE and LSE regions recrystallise separately and their kinetics are independent. The grains recrystallising within LSE regions nucleate at a later stage and their growth is faster. The overall kinetics show a mean behaviour resulting from the contribution from both HSE and LSE regions.

3.3.2. Texture formation as a function of parent grain

Regarding the texture formation, Fig. 7b-c shows the texture ODFs of the recrystallised grains within the HSE (Fig. 7 b.1-b.2) and LSE regions (Fig. 7 c.1-c.2) at the end of recrystallisation for the two alloys – for a limited number of grains, N = 280 – 630. Circles at Fig. 7a designate where the texture plots correspond in the growth process. In both alloys, recrystallisation initiates in the HSE regions. The high local disorientation within these regions suggest high dislocation density that provides the necessary driving force to initiate recrystallisation [2]. Indeed, in the binary alloy recrystallisation was observed to initiate and grow dominantly from the HSE regions (Fig. 4a). Moreover, as it was seen earlier, the recrystallisation texture evolution showed that the {111}⟨112⟩ component increased significantly towards the latter stages of recrystallisation, at about

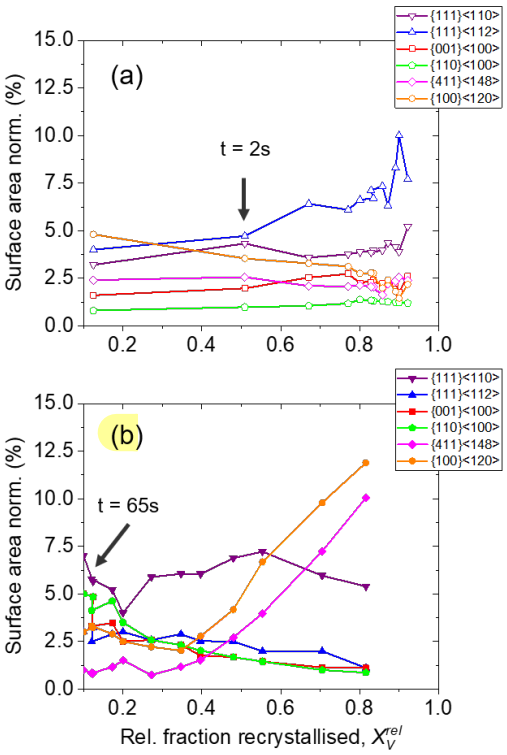

Figure 5: The evolution in normalised surface area of the main annealing texture components during sequential heat-treatment at 700° C for a) binary (open points) and b) ternary alloy (solid points) taking into account all the new grains. Arrows on the plots designate the stage when recrystallisation proceeds in the low-stored energy regions.

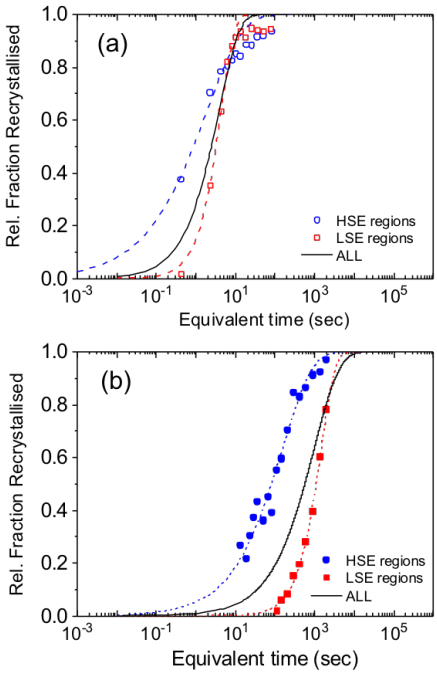

Figure 6: Microstructural experimental data for recrystallisation from sequential EBSD the recrystallisation kinetics for the two alloys after separating the deformed state into HSE (blue squares) and LSE (red circles) regions for a) binary (open points) and b) ternary (solid points) alloys.

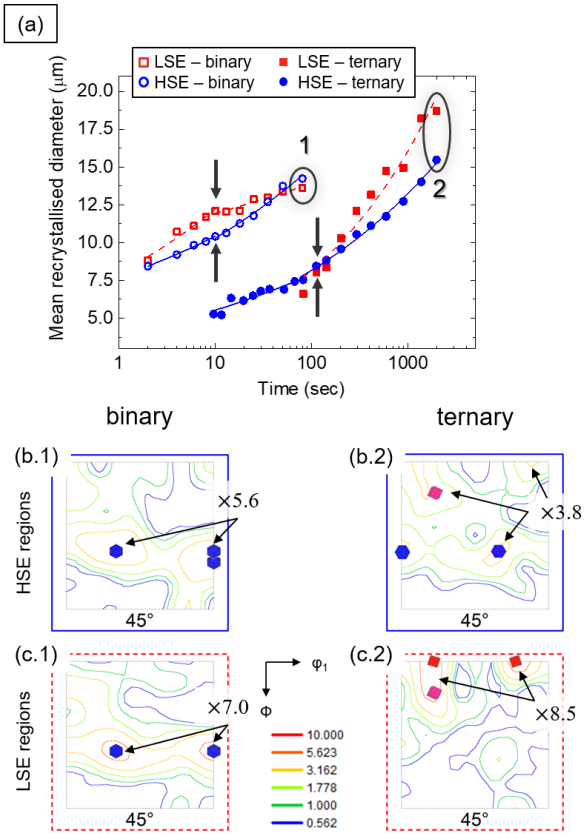

Figure 7: Evolution of microstructure in the high (HSE) and low stored energy (LSE) regions respectively, a) the growth of new grains with annealing time for binary (open points) and ternary (solid points), arrows indicate the stage when recrystallisation proceeds in the LSE regions. The micro-texture ODF plots at the ϕ_2 = 45°section of the Euler space of the new grains at the end of recrystallisation as a function of parent grain: for binary b.1) HSE (N=631), c.1) LSE (N=386) and for ternary b.2) HSE (N=328), c.2) LSE (N=282), respectively.

$X_V^{rel} = 0.7$. This corresponds to a stage at which recrystallisation is completed in the HSE regions and is expanding into the LSE regions, arrows on Fig. 5 indicate the point where recrystallisation proceeds in the LSE regions. Recrystallised grains from the HSE grow into the LSE consuming these regions. This can be observed in Region 'A' of Fig. 4a where some grains from a recrystallised HSE region are migrating into an adjacent LSE region as recrystallisation progresses in the binary alloy. This behaviour shows characteristics of strain induced boundary migration (SIBM) mechanism as will be discussed more extensively in a following section. Thus, in the binary alloy a similar texture is observed after recrystallisation in both HSE and LSE regions as shown in Fig. 7b.1 and c.1. This leads to a peak at the {111}⟨112⟩ component of the γ -fibre with an area fraction almost twice that of the other orientations.

Fig. 7c shows the texture evolution as a function of parent orientation for the ternary alloy. Despite that the HSE regions also recrystallise first, the onset of recrystallisation occurred after a prolonged incubation period and kinetics is particularly sluggish in these regions. In general, the {111}⟨112⟩ orientation in the recrystallisation texture of the ternary alloy stays at low values. Recrystallised grains from HSE regions

show a weak γ-fibre with the peak intensity shared between the $\{111\}\langle 110\rangle$, $\{411\}\langle 148\rangle$ and slightly deviated $\{001\}\langle 120\rangle$ components (Fig. 7b.2).

At a later stage, LSE regions were observed to recrystallise independently. The point when recrystallisation started in LSE regions is indicated by the arrow on Fig. 5b. The recrystallisation of LSE in the ternary alloy was accompanied by an increase in the $\{001\}\langle 120\rangle$, $\{411\}\langle 148\rangle$ and $\{111\}\langle 110\rangle$ orientations, as shown in Fig. 5b. Towards the end of recrystallisation, recrystallised grains from the LSE regions (Fig. 7c.2) show a strong maximum on the θ-fibre and near the $\{h11\}\langle 1/h\ 1\ 2\rangle$ fibre first reported by Homma et al. [45], with a peak intensity of $\times$ 8.5 random near $\{611\}\langle 16\ 12\rangle$. The texture illustrates that the recrystallisation of HSE and LSE regions in the ternary alloy occurs independently as the kinetics have shown (Fig. 6b). The ternary recrystallisation texture shows thus, a clear texture inheritance from the parent grain orientation.

In conclusion, the segmentation of the EBSD dataset into HSE and LSE regions revealed that due to Sn addition the two alloys behave very differently in the progress of recrystallisation with respect to the strain heterogeneity of the as deformed state.

3.4. Segregation

3.4.1. Prior grain boundaries

As a starting point, solute segregation was investigated at the prior GBs (PGBs). The material after intermediate annealing, i.e. before cold rolling, was preferred for characterization since the cold deformed state was found to be quite brittle for APT analysis. Fig. 8a shows the EBSD ROI from which a random GB, $\theta = 28°[123]$ was selected for chemical analysis, views of the APT volume containing the PGB of interest are shown in Fig. 8b. In the APT volume, all Sn atoms (green spheres) are shown and for simplicity the Fe matrix atoms are only partially shown. The concentration profile for Sn across the GB is given in Fig. 8c. APT analysis revealed a segregation amount of Sn of 2.3 at.nm^{-2}. Additionally, interstitial C and B atoms were observed to segregate at this boundary, although both were at residual levels in the nominal composition of these alloys. Segregation of C and B is considered to occur also in the binary grain boundaries and is thought to exert negligible solute drag effects. Nonetheless, site competition and potential interaction of these elements with Sn atoms cannot be dismissed, especially in the case of C and Sn [24].

3.4.2. Onset of recrystallisation

After the thorough examination of the recrystallisation orientation preferences and kinetics with the addition of Sn, it is evident that the HSE regions are of great importance. Therefore, the substructure of a HSE region of the ternary alloy was further investigated. The EBSD characterization of the ND–RD section (Fig. 9), revealed that the HSE region had a finer intragranular cell-structure of subgrains, while LSE regions were considerably coarser. If the subgrain model of Cahn [3] is assumed to describe the mechanism of nucleation of recrystallised grains, a nucleus derives from a successful subgrain that grows

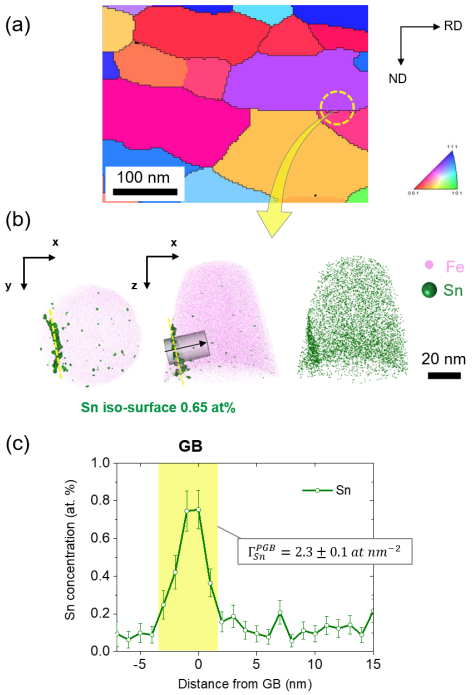

Figure 8: The ternary alloy prior to cold rolling a) EBSD ND-IPF mapping of the microstructure (black lines representing GBs with 15 – 65°misorientation), b) different views of the APT volume with Sn segregation (green spheres) at the prior GB, c) the concentration profile for Sn perpendicular to the interface.

during the incubation period. Markedly, these regions of the microstructure are very important to understand the nucleation mechanisms. Fig. 9a shows the EBSD GAM map at the onset of recrystallisation in the ternary material ($X_V \sim 0.07$). The fine subgrain structure inside the deformed grain can be observed, along with the presence of a recrystallised grain having very low intra-granular misorientation variation. The recrystallised grain represents the successful nucleation process from subgrain growth selectivity. Subgrain boundaries (SGBs) at the onset of recrystallisation were analysed with APT after isothermal holding equivalent to 1.6 seconds at 700° C. Fig. 9a-b shows the EBSD ND-IPF maps of the material at different magnifications, and the mint green circle shows the region of subgrain structure from which a tip for APT was prepared by FIB–SEM. The orientation of the parent grain area is near $\{111\}\langle 110\rangle$ along the γ-fibre. The APT analysis revealed the presence of a triple junction between three SGBs, in Fig. 9c, Sn atoms are represented as green spheres. Remarkably high Sn segregation was observed to decorate the SGBs already at this very early stage of recrystallisation. Besides Sn atoms, no other element was found to meaningfully segregate at the SGBs. Si concentration shows some variation at the boundary but the enrichment factor (concentration at boundary over the concentration at the bulk) is near unity and is thus considered negligible.

The segregation profiles of Sn across the different SGBs are shown in Fig. 10a. The segregation was quantified with the Gibbsian excess number (Fig. 10b) and was found to be different for the three SGBs: 2 interfaces are found to have similar amount of Sn, SGB1 0.91 and SGB3 0.94 at.nm^{-2} while the

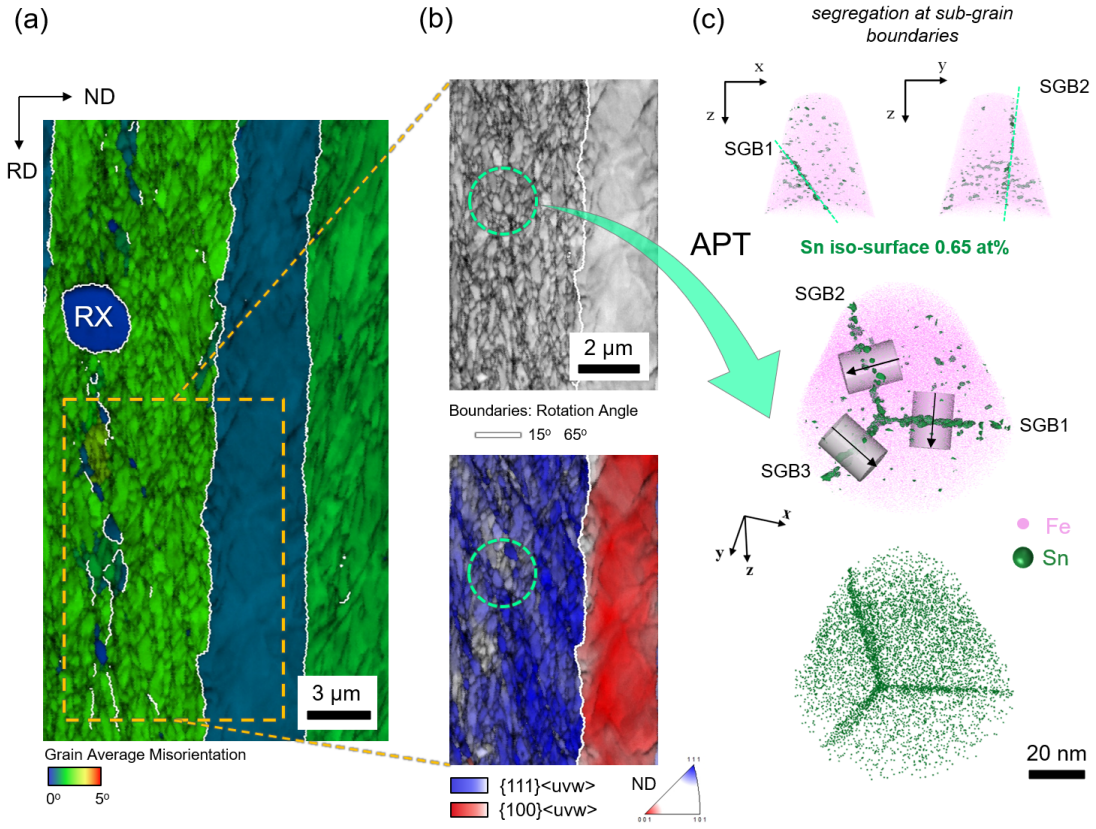

Figure 9: The ternary alloy at the early stages of recrystallisation ($X_V = 0.07$) analysed in EBSD before APT analysis. EBSD maps shown at various magnifications with the region of interest where the APT tips were taken from (mint-green circle) a) GAM+IQ map, b) IQ map and orientation colored map showing the grains with {111} and {100} parallel to ND, c) different views of the APT volume with Sn segregation (green spheres) at the subgrain boundaries.

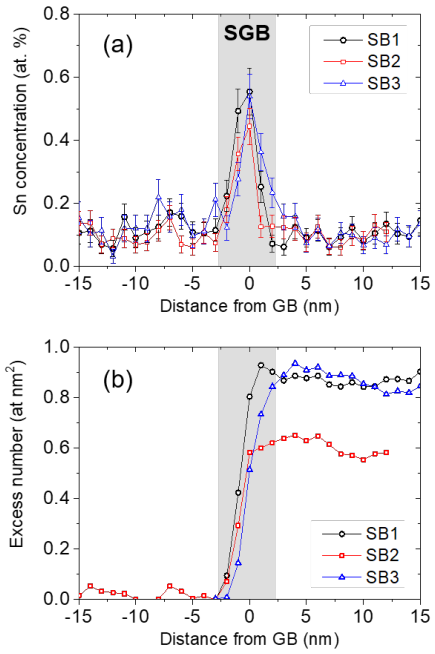

Figure 10: (a) the concentration profiles perpendicular to the interface for the subgrain boundaries and (b) integral profiles that yield the Gibbsian excess number at each SGB.

other one, SGB2, has a lower amount of Sn of 0.59 at.nm^{-2}. The Sn segregation is probably varying depending on subgrain angle, as Read and Shockley observed for low-angle boundaries [46]. Additionally, a segregation misorientation dependence has been previously reported for Sn for a binary Fe-Sn alloy [47]. Unfortunately, the exact misorientations associated to the SGBs were not accessible as the ROI was very small and it was challenging to control the exact location during FIB sample preparation. Nevertheless, by segmenting the EBSD map to include only the not recrystallised structure of that particular prior grain, it was found that nearly 75% of the SGBs had a misorientation $2.5° \leq \theta < 9.5°$, while the mean value was, $\theta = 8.2°$. Hence, statistically it is reasonable to assume that the analysed SGBs may have a misorientation near these values.

Maruyama et al. [48] have also observed Nb solutes at subgrain boundaries of a Fe-Nb alloy at the stage of recrystallisation incubation and the excess number is comparable at about 1.19 at.nm^{-2}.

4. Discussion

The as deformed microstructure constitutes the initial state and will define the path for the thermally activated phenomena that will take place during annealing. Thus, it is important to have a good understanding of the microstructure at this

stage. The alloys were cold rolled at a true strain of about ϵ = 2. At these large levels of strain, the deformed microstructure is known to be comprised of a well-defined network of subgrains [2]. The subgrain structure is formed by dislocation accumulation arranged in a cell like structure in the grain interior [49]. The dislocation arrangement within the deformed grains differs with grain orientation as the energy of deformation is known to be stored heterogeneously across different orientations [16]. It is suggested that subsequent nucleation of recrystallisation proceeds in an orientation-dependent manner [17]: for cold rolled metals, recrystallisation takes place primarily in orientations with high stored energy [18]. More specifically, according to the Taylor factor criterion, the {110}⟨110⟩ orientation (at Φ = 90° of the α-fibre) is expected to demonstrate the highest capacity to store the energy of deformation [16]. However, such orientation is scarcely observed in the cold rolled microstructure of conventionally processed single-phase α-Fe [50]. In cold rolled α-Fe the most abundant, high Taylor factor orientations, are {111}⟨*uvw*⟩ (γ-fibre) orientations. During rolling, the {111}⟨*uvw*⟩ grains exhibit higher slip activity than the other orientations and as a result store higher amount of energy during deformation. In particular, the {111}⟨112⟩ oriented grains are prone to form shear bands during deformation [51]. On the contrary, the {001}⟨110⟩ (at Φ = 0°of the α-fibre) component are the lowest dislocation density grains [16]. Therefore, during recrystallisation of the cold deformed materials, the {111}⟨*uvw*⟩ grains usually recrystallise readily, while the {001}⟨110⟩ orientations are more reluctant to recrystallise [22].

The sequential EBSD experiments showed that the solute addition altered markedly the recrystallisation preferences. In brief, it was observed that during annealing, HSE regions recrystallise promptly without Sn addition however, when Sn is added, the onset of recrystallisation is greatly retarded in these regions of the as deformed microstructure. A distinct difference observed in the ternary alloy is that LSE regions recrystallise independently at a later stage of the process. As a result, the recrystallized texture is weaker compared to the binary alloy and the presence of some {001}⟨*uvw*⟩ texture components are also observed.

Overall, the texture observations made from the sequential EBSD experiment are in accordance with *ex situ* observations [34], where the analysis of several thousands recrystallized grains showed that Sn is affecting significantly the recrystallisation texture from the onset. Additionally, the overall recrystallisation kinetics of the two alloys, shown in the global study [34], displayed the same retardation of recrystallisation nucleation with the addition of Sn shown in the present work. In section 3.2.1, we saw that the recrystallisation kinetics of HSE and LSE regions in the ternary alloy showed a distinct change in the JMAK exponent.

In an earlier study [52], we have reported the segregation of Sn at half-recrystallisation in migrating GBs. Here, the focus is shifted to the very beginning of recrystallisation and the initial segregation state. The retardation of recrystallisation in the HSE regions, in the presence of Sn, was identified to be a key point to understand the solute effect on texture evolution. Hence, such regions were selected to perform a site-specific chemical analysis. Sn segregation was measured with APT at SGBs of the non-RX structure within a substructured HSE region (within a {111}⟨110⟩ oriented region). The APT analysis revealed a remarkably high Sn segregation decorating the SGBs at the onset of recrystallisation, shown in Fig. 9. This experimental finding of Sn segregation at this early stage of recrystallisation, is of great importance for understanding how the nucleation of recrystallisation may be affected by segregation. All segregation data measured at different stages of recrystallisation, reported here and in previous works, are summarised in Table 2 together with crystallographic information. First, we should consider the diffusion processes involved.

4.1. Diffusion of Sn to subgrain boundaries

The segregation results showed that a swift annealing of 1.6 seconds at 700° C was sufficient for Sn solutes to segregate at SGBs of the non-RX structure with levels of 0.6-1 at.nm^{-2}. Hence, this raises the question of the diffusion mechanism that transported the Sn atoms so efficiently to the SGBs. SGBs consist of dislocation accumulation, initially they are created due to the large strain applied during cold deformation; at this stage, Sn atoms should be mainly in solid solution in the grain interior prior to the recrystallisation annealing and the SGBs should not be solute enriched. Sn atoms are considered to be in solid solution in the grain interior at t = 0. Nevertheless, during annealing below the recrystallisation temperature, the dislocations at the SGBs tend to re-arrange via dislocation glide and climb. The authors have previously discussed that Sn solutes could already affect dislocation motion and retard the subgrain formation during recovery processes [31].

Making these assumptions (no segregation of Sn at SGBs at t = 0), kinetics can be calculated tacking into account diffusion from the grains to the SGBs and assuming local equilibrium between grain and SGBs. Indeed, it is usually assumed that during segregation, a local equilibrium between the GB and its vicinity is attained since the time required to equilibrate the GB should be faster compared to the time needed for diffusion from the grain interior that controls the concentration at the GB vicinity. Moreover, the temperature dependence of grain boundary segregation can be described by the Langmuir-McLean isotherm. To account for these conditions and following the analysis of Fournier Dit Chabert et al. [53], the segregation kinetics of Sn was calculated by finite difference simulation in one dimension using: *(i)* the second Fick law for the bulk diffusion in the grain, and *(ii)* the Langmuir- McLean isotherm to calculate the local equilibrium between the GB and its vicinity. A segregation energy at random GBs at 700° C, ΔG^0_{Sn}= -51.3 kJmol^{-1} and a site saturation x^0_{Sn}= 1/3 were used as reported for Sn in α-Fe in [54]. The segregation kinetics were calculated for a semi-finite volume with a half interface and half grain [53]. A GB width, δ=0.5 nm was selected as in the study of Inoue et al. [55]. For the purpose of the present simulation the subgrain width is assumed to be comparable to grain boundary width [42]. The grain with a half grain size[1], x= 300 nm was divided in ele-

[1] the half grain size, x= 300 nm was selected as this value corresponds to the half of the mean subgrain size, $d_0/2$ experimentally observed in the ROI.

Table 2: Data on segregation of Sn during different stages of recrystallisation. Grain boundary crystallographic information as obtained from the EBSD orientation mappings and the values of interfacial segregation for Sn, Γ_{Sn}^{GB} as analysed with APT.

	Adjacent grains	Euler Angles (ϕ_1, Φ, ϕ_2)	Boundary	Grain boundary, θ [h,k,l]	Interfacial excess of Sn (at. nm^{-2})	Ref.
Prior to cold rolling	Grain 1 Grain 2	31°, 52°, 43° 28°, 26°, 63°	Grain 1/ Grain 2	random GB, 28°[123]	2.3 ± 0.1	This work
Recrystallisation incubation	Subgrain 1 Subgrain 2 Subgrain 3	matrix: 0°, 55°, 45°	SGB 1 SGB 2 SGB 3	–	0.91 ± 0.09 0.59 ± 0.04 0.94 ± 0.08	This work
Recrystallisation migration	RX Grain 1 RX Grain 2 Non-RX matrix	13°, 32°, 40° 49°, 27°, 21° 30°, 55°, 44°	Grain 1/ Non-RX Grain 2/ Non-RX	random GB, 48.2°[4 -1 2] random GB, 27.5°[-4 3 2]	0.60 ± 0.08 0.41 ± 0.06	[52]

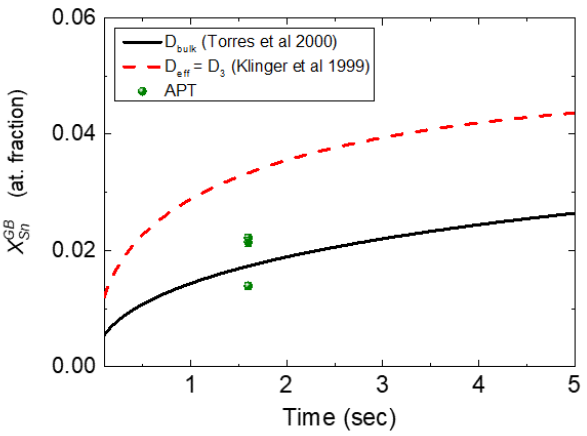

Figure 11: Kinetics of Sn segregation at the grain boundaries compared to the experimental APT values of Sn at subgrain boundaries and changing the diffusion coefficient from D_{bulk} [56] to an efficient diffusion coefficient D_{eff}=D_3 [57].

ments with a size equal to half the GB size, dx= 0.25 nm. Diffusion in the grain was solved by explicit finite difference using the second Fick law in one dimension. At each time step of the diffusion with the finite difference simulation, the Sn concentrations in the SGB and in the grain element in contact with the GB were equilibrated using the Langmuir- McLean equation and the conservation of mater. Note that under these assumptions, the kinetics of segregation is mainly controlled by the diffusion in the grain but depends also on the equilibrium segregation that fix the boundary condition at the grain/SGB interface.

Fig. 11 shows the segregation kinetics of Sn segregation to the GBs (or SGBs) from the APT segregation data and the calculated segregation kinetics. In the case of pure bulk diffusion of Sn atoms from the bulk to the SGBs (Fig. 11 solid line), the diffusivity of Sn in α-Fe below the Curie transition temperature was reported by Torres et al. [56] as:

$$D_{bulk} = 3.5 \cdot 10^{-2} \exp(\frac{-275000}{RT}) \quad \text{m}^2\text{s}^{-1} \qquad (1)$$

using the $D = D_{bulk}$, the predicted segregation amount correlates well with the APT measured values of Sn segregation. In other words, the diffusion length, $\sqrt{D_{bulk} \cdot t}$ for pure bulk diffusion could explain the Sn atom transport to the SGBs at the onset of recrystallisation.

Nevertheless, acknowledging the large amount of cold strain applied, the short annealing time and the fact that the APT analysis was performed in the interior of a high dislocation density region, it is reasonable to assume that dislocations may have a contribution to the overall diffusivity of Sn atoms. Diffusion through dislocation pipes is considered to have a diffusion coefficient of up to three orders of magnitude, in the case of pure pipe diffusion, higher compared to bulk diffusion [58, 59, 16]. In the current circumstances, it is more appropriate to think that the transport of atoms is controlled by an effective diffusion coefficient, D_{eff} which incorporates both the contributions from pipe and bulk diffusion [60]. Klinger et al. [57] and more recently Divinski et al. [61], have given a theoretical basis for the D_{eff} variance with the individual contributions. For instance, dislocation enhanced diffusion has been discussed for its importance in the diffusion of Nb in α-Fe [61].

In these works, the bulk diffusion coefficient in the classical model from Fisher of GB diffusion, is substituted by $g_d D_d$, where g_d is the volume fraction of sites belonging to dislocation pipes. Then D_{eff} is expressed as:

$$D_{eff} = D_3 = g_d D_d + (1 - g_d) D_{bulk} \qquad (2)$$

g_d in Eq. 2 is calculated using the dislocation density of the as deformed state for the $\{111\}\langle 110\rangle$ orientation, $\rho = 10^{-15}$ m^{-2} as reported in a previous study from EBSD data [31]. It is noted that the D_3 diffusion coefficient is an approximation as the dislocation density used here represents the total number of geometrical necessary dislocations (GND) estimated from EBSD data. In principle, the relevant dislocations in the case of efficient diffusion would be the ones within the bulk, subtracting from the total density the dislocations that form the subgrain walls. A detailed assessment of such diffusion mechanism is complex. More segregation data at different annealing times are needed. Additionally, dislocation density data regarding mobile dislocations from the grain/subgrain interior and as a function of crystallographic orientation would be essential.

In comparison to the APT experimental data at the onset of recrystallisation, the dashed line in Fig. 11 shows that segregation kinetics with an efficient diffusion in the D_3-regime, can be considered to be relevant as well in the present conditions. Nonetheless, further work will be needed in this direction.

4.2. Texture evolution with Sn

4.2.1. Recrystallisation affected by segregation

With respect to the recrystallisation texture development, the observed segregation is also central. The presence of Sn at SGBs can explain the retardation of recrystallisation by decreasing the rate of subgrain coarsening due to solute drag pinning. The HSE regions should be more affected by Sn segregation at the SGBs, since hard Taylor factor orientations tend to form a finer substructure during deformation and to contain a higher density of intra-granular defects.

We have observed that the binary alloy recrystallises mainly from the grain interior of the $\{111\}\langle uvw\rangle$ prior grains producing a strong $\{111\}\langle uvw\rangle$ texture. Essentially, the recrystallisation mechanism in these regions is the one introduced by Cahn [3]; a successful recrystallisation nucleus is formed during subgrain coarsening processes. Several possible mechanisms may come into play during recrystallisation to assist the subgrain formation and coarsening [62]: *(i)* recovery phenomena, rearrangement and accumulation of dislocations at the SGBs; *(ii)* subgrain coalescence phenomena via migration of low angle boundaries increasing gradually their misorientation with the matrix. Static recrystallisation of HSE regions, usually promotes a strong $\{111\}\langle uvw\rangle$ recrystallisation texture well known in low carbon steels [22, 21]. Similarly, in our binary alloy, recrystallisation proceeds heterogeneously with the HSE regions reaching full recrystallisation whilst nucleation is still not initiated in the LSE. Eventually, there is a critical time for which the dislocation density in the LSE regions becomes higher than in the recrystallised HSE regions. This dislocation density difference provides the driving force for the recrystallised grains of HSE regions to migrate into the LSE regions. Such recrystallisation process is known as strain induced boundary migration (SIBM) or GB bulging. It occurs as a crystal within a lower dislocation density region is favoured to grow into an adjacent region with a higher dislocation density [5, 63], once a critical size and dislocation density difference is acquired [64]. The role of SIBM during static recrystallisation has been previously reported in the literature [17, 65, 66]. An example of SIBM can be observed in the sequential EBSD mappings of the binary alloy Fig. 12. The region 'A' shows the recrystallisation between a HSE and a LSE region separated by a prior GB. It is observed that after HSE regions are fully recrystallised, recrystallised grains from the HSE regions bulge into the sluggish LSE regions – yellow arrows in Fig. 12 indicate grains which bulge into LSE. The majority of grains migrating into adjacent LSE regions had the $\{111\}\langle uvw\rangle$, consisting about 75% at $t = 2s$, 72% at $t = 4s$, 65.5% at $t = 6s$ of the migrating grains. From these, were often $\{111\}\langle 112\rangle$ grains, about 45% at $t = 2s$, 44% at $t = 4s$, 38% at $t = 6s$, respectively. As a consequence, the recrystallisation texture in the binary alloy is dominated by $\{111\}\langle uvw\rangle$ texture components, which nucleated faster in the HSE regions and grew to consume adjacent LSE regions (see Supplementary Material).

On the other hand, the recrystallisation with Sn addition is seen to be completely different. Segregation at the onset of static recrystallisation, at the substructure of the non-RX HSE regions, is of great importance for understanding how the nucleation is affected by segregation. In the most accepted subgrain boundary model, by Winning et al. [67], the movement of such boundaries occurs through dislocation climb facilitated by vacancies. The physical concept relates to the vacancy motion, which must first escape from the Sn atoms (overcoming the Sn-vacancy binding energy) so that subgrain boundary dislocations can climb [68, 67]. It is suggested that segregated Sn at this stage, will pin subgrain coarsening. Such an effect of Sn in Cu-Sn alloys was assumed also by Cram et al. [68], who modelled and tested the deformation behaviour of the alloys with various Sn contents during dynamic recrystallisation. In consequence, recrystallisation nucleation selectivity, as described by Cahn nucleation model [3] is retarded due to segregation.

Subsequently, as recrystallisation advances, Sn grain boundary segregation is exerting a drag force at the migrating boundaries of recrystallisation retarding the growth of recrystallised grains and the consumption of the non-RX matrix [52]. Hence, nucleation of new grains in the ternary alloy is delayed as evidenced in the number of recrystallised grains at similar X_V and areas of analysis, Fig. 3. The segregation data in Table 2 show that the amount of segregated Sn at the SGBs is higher than the one measured for later stages of recrystallisation on migrating HAGBs. This observation is somewhat unexpected and is considered to be due either to desegregation of Sn occurs for longer annealing at 700° C or to impurity C atoms and site competition for segregation [24].

Furthermore, SIBM events of $\{111\}\langle uvw\rangle$ recrystallised grains into LSE regions is less often observed in the ternary alloy. The reason for this observation could be understood, *(i)* as the size criterion for the subgrains and dislocation density difference does not fulfil the Bailey - Hirsch threshold (Suppl. Mat.) and *(ii)* as Sn enrichment at the PGBs would induce a solute drag effect and could potentially limit GB bulging. For the latter to be valid, some Sn segregation should remain at the PGBs during subsequent cold deformation and recrystallisation annealing. This still remains to be experimentally verified. Additionally, the effect of initial grain size (which was finer for the ternary alloy) would also have favoured SIBM effect if solute drag was not acting on the PGBs.

The overall effect of Sn solute segregation at the prior grain boundaries, subgrain boundaries and recrystallisation interfaces experimentally observed (Table 2), contribute in a significant texture softening compared to the binary alloy. The recrystallised grain intensity of $\{111\}\langle uvw\rangle$ is reduced (nucleation effect), and $\{h11\}\langle 1/h\ 1\ 2\rangle$ intensity increases.

4.2.2. Role of parent grain orientation and formation of $\{h11\}\langle 1/h\ 1\ 2\rangle$ recrystallised orientation

To understand the formation of such texture we must first consider its origin. Deformed grains with $\{411\}\langle 148\rangle$ orientation may form within $\{112\}\langle 110\rangle$ and $\{001\}\langle 110\rangle$ crystals (main components of the LSE regions), where weak lattice curvatures are created at the vicinities of grain boundaries [69]. $\{411\}\langle 148\rangle$ regions in the deformation texture are often regarded to form after severe rolling reductions (i.e. higher than 90%). At large

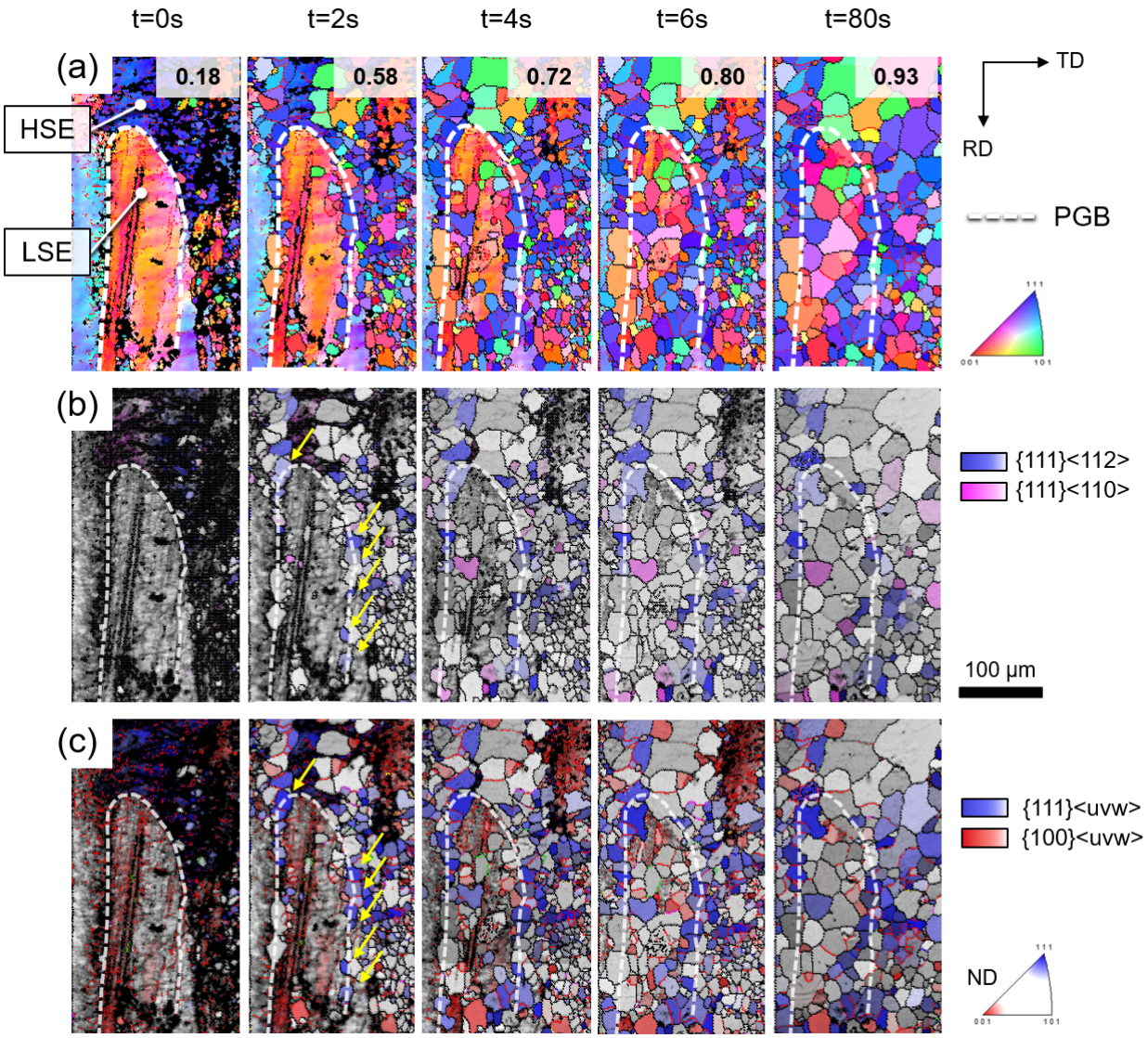

Figure 12: Magnified region of interest 'A' delimited by a white rectangle within Fig. 4a of the binary alloy, showing the interaction of high-stored energy (HSE) and a low-stored energy (LSE) region in the as deformed microstructure as recrystallisation advances at 700° C in the binary Fe-Si alloy. a) ND-IPF mappings, orientation colored maps with IQ: b) for texture components {111}⟨112⟩ and {111}⟨110⟩, c) for texture fibres {111}⟨*uvw*⟩ and {100}⟨*uvw*⟩. High-angle grain boundaries are shown in black and a prior grain boundary is shown with a white dashed line (PGB). At $t = 2s$ yellow arrows indicate recrystallised grains originated in the HSE regions adjacent to the PGB, which migrate into the LSE region during static recrystallisation via stress induced boundary migration (SIBM).

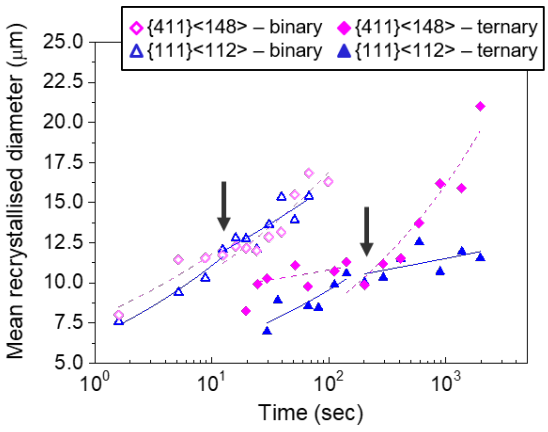

Figure 13: The growth of the most dominant texture components, {111}⟨112⟩ in HSE and {411}⟨148⟩ in LSE for binary (open points) and ternary alloy (solid points).

strains {112}⟨110⟩ and {001}⟨110⟩ regions, near crystal boundaries, can locally fragment and form deformation bands near the {411}⟨148⟩ component [45, 69] or the {311}⟨136⟩ component as reviewed by Gobernado et al. [70, 71]. These intra-granular regions, can store more energy during deformation than the surrounding {001}⟨110⟩ parent grain [72] and thus serve as potential recrystallisation sites within these regions. For the sake of clarity, the {411}⟨148⟩ orientation ($\phi_1 = 20°$, $\Phi = 20°$, $\phi_2 = 45°$) and its vicinity orientations such as the {311}⟨136⟩, will be referred to as the representative component, *R component*, after Gobernado et al. except if the precise orientation needs to be specified [70].

Studies on the recrystallisation of IF steels, confirm that mainly the *R component* is observed after recrystallisation associated with the LSE regions and particularly the deformed {001}⟨110⟩ orientation [22]. Gobernado et al. suggested that the formation of the *R component*, during recrystallisation in a cross-rolled IF steel, is related to oriented nucleation [70], as it was initially suggested by Homma et al. [45]. Whereas, oriented growth theory has also been applied to explain the appearance of this texture component [73], as it has a 26.5°⟨110⟩ misorientation in respect to as deformed {112}⟨110⟩ regions present in the cold rolled state. The increased mobility of 26.5°⟨110⟩ boundaries in bcc metals (Ibe and Lücke model) could assist the selective growth of orientations that these interfaces bound. In a recent study using *in situ* EBSD experiments, Takajo et al. studied the formation of Cube oriented grains ({001}⟨100⟩), which nucleated in the {411}⟨148⟩ as deformed regions and grew preferentially [74]. Thus, the sequential aspect of the recrystallisation evolution presented here, adds a valuable insight on texture development in LSE regions and its origin.

The evolution of the individual texture components in the binary and the ternary alloy (Fig. 5), in combination with the mean growth of the recrystallised grains in HSE and LSE regions (Fig. 7), indicated a different mechanism during recrystallisation. It was observed that the parent grain orientation is decisive, in particular for Sn addition. LSE regions with Sn were observed to recrystallise independently during the progress of recrystallisation due to the Sn solute drag at the HSE regions. It is interesting to consider the grain growth kinetics of the dominant orientations in the primarily recrystallised structure as a function of parent grain orientation. Fig. 13 shows the growth rates of the main texture components, {111}⟨112⟩ for the HSE and {411}⟨148⟩ for the LSE regions of the binary and ternary alloys.

In the binary microstructure, both texture components are observed to have similar growth rates of the mean recrystallised grain diameter (Fig. 13). However, as observed before, the overall intensity of the {111}⟨112⟩ is the most dominant in the recrystallised microstructure. In the ternary alloy, HSE regions are also the first to recrystallise but overall Sn segregation is considered to retard greatly the nucleation in these regions. Then, at a later stage, LSE regions start to recrystallise to form mainly {411}⟨148⟩ (and {100}⟨120⟩) grains. The recrystallisation of the LSE regions, is considered to benefit from recovery processes. Indeed, since LSE regions have a relatively lower dislocation density, their coarsening rate should be faster than in the HSE regions as a result of a coarser structure at the as deformed state and a lower recrystallisation nucleation density. In other words, it can be considered that these regions can potentially coarsen more readily during annealing. Duggan and Roberts [75] studied texture evolution after extensive recovery and subsequent recrystallisation in a low carbon steel and they observed a strong {411}⟨148⟩ texture component in the annealing texture. Essentially, the {411}⟨148⟩ component grew faster as it nucleated in LSE zones where the nucleation density is lower, thus grain growth competition and impingement are reduced. In contrast, in the HSE zones the high nucleation density results in sooner impingement, which reduces the recrystallised growth in these regions. Fig. 13 demonstrates these microstructural considerations during the sequential recrystallisation.

Fig. 14 focuses on the recrystallisation of the LSE regions in the microstructure of the ternary alloy. The main texture component observed after recrystallisation of these regions was the *R component*; the peak is observed at {611}⟨16 12⟩ ($\phi_1 = 20°$, $\Phi = 13°$, $\phi_2 = 45°$) this orientation is near the {411}⟨148⟩ ($\phi_1 = 20°$, $\Phi = 20°$, $\phi_2 = 45°$) component. It is observed that the *R component* was one of the first orientations to recrystallise. Its formation occurred mainly at the vicinity of low-angle GBs, designated by red arrows in Fig. 14. Towards the end of recrystallisation, grains of the θ-fibre, near the {001}⟨120⟩ appear as well (Fig. 14b). Recrystallisation in the LSE regions, may also be assisted by subgrain coalescence phenomena. Such an example can be seen within a region of interest 'B' in Fig. 14a, with recrystallised grains appearing in microbands oriented near the *R component*. Recrystallised grains within region 'B', are products of low-angle rotations and nucleate at the vicinity of a LAGB with an orientation relationship of 9°⟨110⟩ with the as deformed matrix. The recrystallisation retardation due to the solute segregation at SGBs and recrystallisation boundaries is believed to favour the LSE regions ({001}⟨110⟩ deformed grains) to recrystallise at a later stage, with an oriented nucleation mechanism. Subgrain coalescence might explain the formation of these recrystallised grains. However, for subsequent growth,

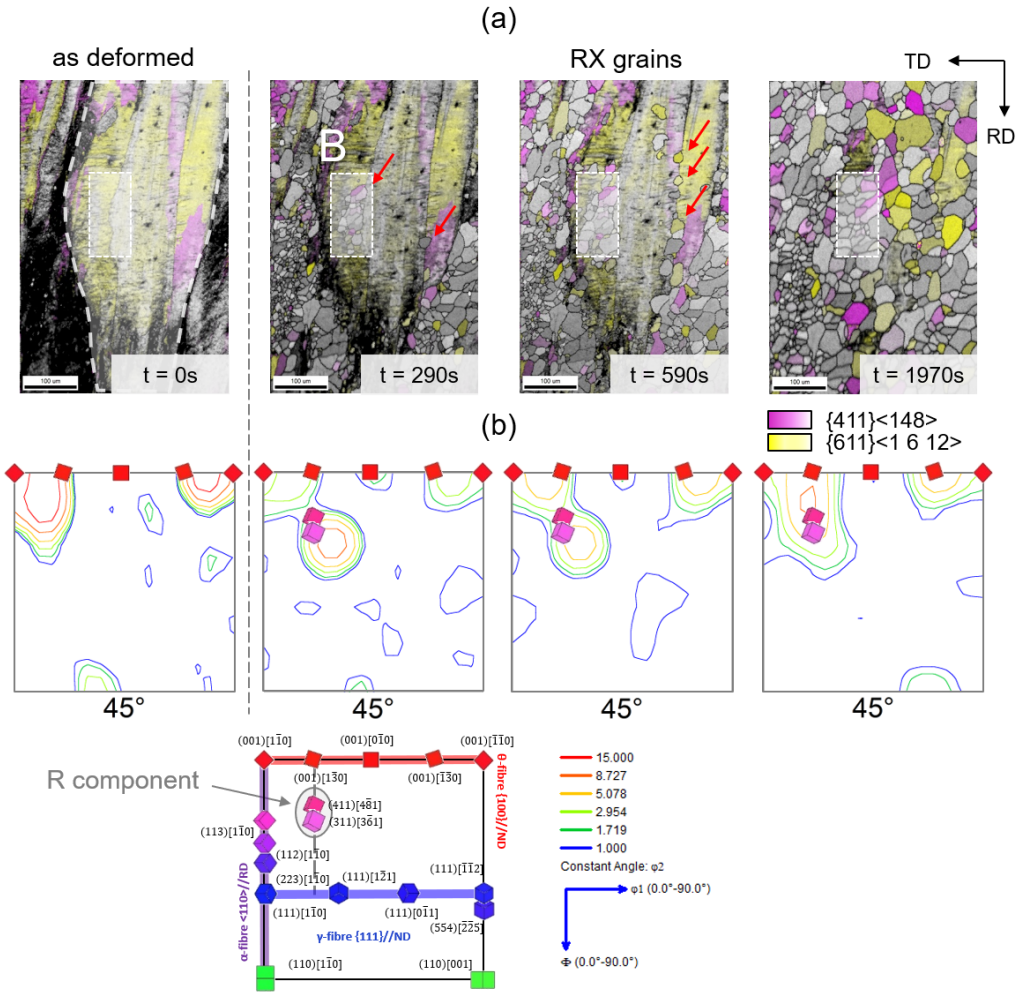

Figure 14: Recrystallisation within a parent near {001}⟨110⟩ grain of LSE regions in the ternary alloy, a) {411}⟨148⟩ and {611}⟨16 12⟩ recrystallised grains highlighted. b) the micro-texture ODFs at the ϕ_2 = 45°section of the Euler space, of only the recrystallised grains. The texture maxima and number of grains analysed are for t = 0s: x24.7 mrd at ϕ_1 = 10°, Φ = 10°, ϕ_2 = 45°(only parent grain) – t = 290s: x12 mrd at ϕ_1 = 29°, Φ = 29°, ϕ_2 = 45°(N = 40) – t = 590s: x8.5 mrd at ϕ_1 = 14°, Φ = 0°, ϕ_2 = 45°(N = 71) – t = 1970s: x9.4 mrd at ϕ_1 = 19°, Φ = 14°, ϕ_2 = 45°(N = 158), respectively.

the presence of mobile boundaries is needed.

4.3. Grain Boundary Mobility

Grain boundary mobility is a necessary criterion for a successful recrystallisation nucleus. Furthermore, it is an asset for already recrystallised grains to acquire a growth advantage [77]. Mobility of all types of boundaries is dramatically affected by solute addition due to solute drag, but the mobility of CSL boundaries may be less affected compared to general GBs. In a previous study, we have discussed the solute drag effect of Sn on the migration of general GBs during recrystallisation [52]. In the presence of solute atoms, the high mobility of low CSL boundaries is believed to be pivotal to the microstructural development, as these interfaces may suffer less drag due to solute grain boundary segregation [11]. Despite that segregation of comparable magnitude is also expected at CSL boundaries by thermodynamics as reported for Sn in α-Fe by Lejček et al. [54].

From the sequential EBSD experiment, the selective growth possibility of the *R component* was evaluated. CSL distributions in both binary and ternary alloys, showed the increased frequency of some Σ ⟨110⟩ type boundaries [78]. Especially during the growth stage of recrystallisation, the fraction of Σ9, Σ19a, Σ33a, Σ33b and Σ11 increased within the polycrystalline structures. These boundaries can potentially promote the growth of γ-fibre orientations by ⟨110⟩ type orientation transformation of α-fibre grains as described by Gangli et. al [18] and computer simulations of orientation selectivity by Kestens et al. [79]. In a re-evaluation of selective growth in bcc steels, Verbeken et al. [73] claimed to have revealed the formation of the *R component* as a selective growth mechanism from the as deformed {112}⟨110⟩ orientations due to the increased mobility of 26.5°⟨110⟩, near the CSL Σ19a boundary.

The misorientation distributions in the recrystallised segmented data were evaluated for the LSE regions in the ternary alloy. In these parent grains, the formation of strong *R component* was observed, which showed a strong correlation with

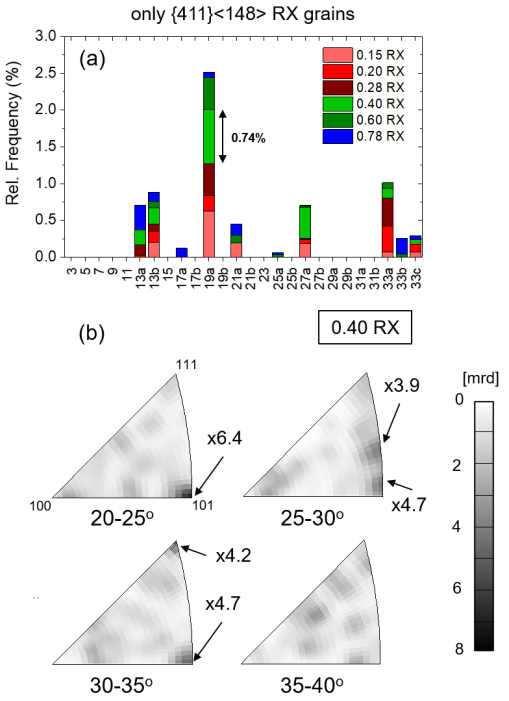

Figure 15: a) The CSL boundary frequency normalised by the random grain assembly [76] and b) misorientation/axes bounding {411}⟨148⟩ recrystallised grains at $X_V^{rel} = 0.4$ in the ternary alloy.

high mobility misorientation/axes known in bcc metals. In particular, the {411}⟨148⟩ component is highly bounded by ⟨110⟩ boundaries. Fig. 15 shows the boundaries of {411}⟨148⟩ recrystallised grains in the ternary alloy as a function of area fraction recrystallised. Fig. 15a shows the CSL frequency of this component normalised by the random grain assembly CSL frequency based on boundary length [76, 80]. From the CSL and misorientation distributions, the highest frequency was observed at 29 – 30°⟨110⟩ near the Σ19*a* (26.5°⟨110⟩) as in Ibe-Lücke's model of selective growth in Fe- 3%Si [81, 19]. Meanwhile, it is interesting to observe that more ⟨110⟩ CSL boundaries were associated with this component, namely Σ27*a*, Σ33*a* and Σ33*b*.

On the other hand, the {611}⟨16 12⟩ component (peak intensity within the LSE region) revealed a high frequency of GBs about 30°⟨111⟩ instead, which is near the Σ13*b* (27.8°⟨111⟩). Sanjari et. al [82] observed a similar behaviour of selective growth of the *R component* having a high frequency of 30°⟨111⟩ GBs. All aforementioned HAGBs could acquire the necessary mobility to assist the growth of the *R component* grains and survive the grain growth process [12, 23]. Perhaps the selective growth of {411}⟨148⟩ due to the near 26.5°⟨110⟩ orientation relationship, might be a key factor in why these grains have shown to dominate the primary recrystallisation texture of the {001}⟨110⟩ parent orientations, as they have been regularly reported to be present in the secondary recrystallised microstructure as well [83].

Recently, Suehiro et al. reported on the effect of Sn during the grain growth following primary recrystallisation of Fe3% Si and with Monte Carlo simulations [84]. They observed that the growth of the {411}⟨148⟩ grains increased when Sn was added, while in contrary the growth of {111}⟨112⟩ grains reduced. These authors attribute the growth behavior with Sn to a difference in solute drag effect on low-angle and high-angle GBs. Such non-isotropic solute drag can potentially be of importance, although the size advantage of the {411}⟨148⟩ grains already acquired from primary recrystallisation should not be overlooked. Grain growth after recrystallisation, essentially is a process during which the larger grains consume the smaller ones. Finally, it is interesting to note that when only the {411}⟨148⟩ grains are concerned Suehiro et al. also observed a peak near the 26.5° misorientation as we report here from the sequential EBSD observations.

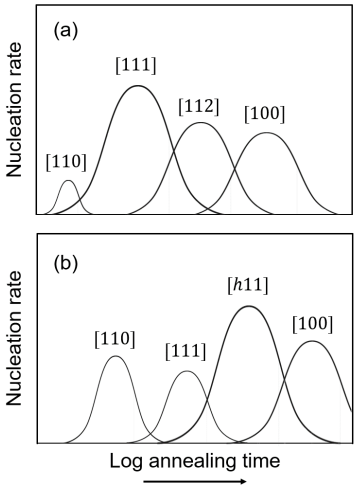

Figure 16: Schematic of recrystallisation sequence in the two alloys constructed from the texture densities and recrystallisation kinetics observations: a) binary (no Sn) similar to [22] and b) ternary, with Sn addition.

Overall, from the recrystallisation observations reported here and previous *ex situ* study, the recrystallisation sequence in the two studied alloys: with and without Sn can be summarised schematically in Fig. 16. Fig. 16a shows the case for the binary alloy (no Sn), which as it was shown here, has a similar recrystallisation behaviour to low carbon steels as proposed by Hutchinson [22]. Fig. 16b shows the sequence in the presence of solute Sn. The schematic is semi-quantitative, including information on the recrystallisation retardation and orientation magnitude proportional to the texture densities measured experimentally taking into account several thousands of grains [34].

5. Conclusions

The static recrystallisation in cold rolled Fe-Si model alloys was investigated with sequential EBSD assessing for the effect of Sn solute addition during recrystallisation annealing. Sn segregation was analysed site-specifically with APT, revealing segregation at different stages of recrystallisation that is crucial in understanding the texture formation. The orientation dependence of stored energy is proven essential for the understand-

ing of texture modification with Sn. As in the case of no Sn, the $\{111\}\langle uvw\rangle$ parent grains were the highest stored energy orientations, while the low Φ angles along the α-fibre and $\{001\}\langle 110\rangle$ were the lowest stored energy orientations. Without Sn, the fastest regions to recrystallise ($\{111\}\langle uvw\rangle$) were observed to dominate the microstructure during recrystallisation and essentially defined the texture.

Recrystallisation texture with the addition of Sn can be summarized in the following. Solute affected significantly the onset of recrystallisation in $\{111\}\langle uvw\rangle$ oriented regions by segregation at the subgrain boundaries of the as deformed/recovering microstructure, prolonging the incubation period. At this stage, Sn segregation was suggested to have a pinning effect during subgrain coarsening and hence, retard the onset of recrystallised grains. Recrystallisation proceeds with parent grains recrystallising independently in the Sn-containing alloy; segregation at prior grain boundaries could be responsible for the reduction of SIBM from faster recrystallising regions. The growth of new grains was dictated by the available stored energy, nucleation density within each parent grain and solute drag of Sn on migrating interfaces. Low stored energy regions recrystallised independently at later stages of the process. Oriented nucleation of $\{411\}\langle 148\rangle$ grains was observed in these regions. Segregation phenomena were shown to promote $\{411\}\langle 148\rangle$ recrystallisation as a consequence of solute drag in as deformed $\{111\}\langle uvw\rangle$ regions. The growth of such grains was one of the fastest observed within the primarily recrystallised microstructure. Ibe and Lücke known theory of selective growth of $26.5°\langle 110\rangle$ boundaries might explain why these grains grew so rapidly.

These results showed that the combination of local chemical element distributions and thermodynamic study with crystallographic analysis can be very insightful and can pave the way towards understanding the active physical mechanisms not only in the Fe-Si system, but may be expanded for other single-phase metals were solute segregation takes place.

Acknowledgements

N.Mavrikakis is grateful for the financial support of the National Association of Research and Technology (ANRT – Project no.1073–2015). Dr. M. Descoins of Institut Matériaux Microélectronique Nanosciences de Provence (IM2NP), Marseille is acknowledged for technical assistance in the APT experiments. N.M. would also like to thank Dr. ir. C. Goulas of University of Twente for his contributions in the final version of the manuscript.

References

[1] M. H. F.J. Humphreys, Recrystallization And Related Annealing Phenomena, 2nd Edition, ELSEVIER Ltd, 2004.

[2] R. D. Doherty, D. A. Hughes, F. J. Humphreys, J. J. Jonas, D. Juul Jensen, M. E. Kassner, W. E. King, T. R. McNelley, H. J. McQueen, A. D. Rollett, Current issues in recrystallization: A review, Mater. Sci. Eng. A 238 (2) (1997) 219–274.

[3] R. W. Cahn, A new theory of recrystallization nuclei, Proceedings of the Physical Society. Section A 63 (4) (1950) 323.

[4] P. A. Beck, Do Metals Recrystallize?, JOM 4 (9) (1952) 979–980.

[5] F. J. Humphreys, A unified theory of recovery, recrystallization and grain growth, based on the stability and growth of cellular microstructures- I The basic model, Acta Met. 45 (1997) 4231–4240.

[6] B. Hutchinson, Nucleation of recrystallisation, Scripta metallurgica et materialia 27 (11) (1992) 1471–1475.

[7] H. Hu, Recovery and Recrystallization of Metals, AIME (L. Himmel) (1962) 311–326.

[8] K. Lücke, K. Detert, A quantitative theory of grain-boundary motion and recrystallization in metals in the presence of impurities, Acta Metallurgica 5 (11) (1957) 628–637. doi:10.1016/0001-6160(57)90109-8.

[9] J. W. Cahn, The impurity-drag effect in grain boundary motion, Acta metallurgica 10 (9) (1962) 789–798.

[10] L. S. Shvindlerman, G. Gottstein, D. A. Molodov, Grain boundary motion in pure metals: Effect of interaction between adsorbed atoms at moving boundaries, Phys. Status Solidi A-Appl. Res. 160 (2) (1997) 419–429.

[11] K. T. Aust, J. W. Rutter, Grain Boundary Migration in High Purity Lead and Dilute Lead-Tin Alloys, Trans. Metal. Soc. AIME 215 (1959) 119–127.

[12] H. Homma, B. Hutchinson, Orientation dependence of secondary recrystallisation in silicon-iron, Acta Materialia 51 (13) (2003) 3795–3805. doi:10.1016/S1359-6454(03)00193-9.

[13] J. Harase, R. Shimizu, N. Takahashi, Coincidence grain boundary and (100) [001] secondary recrystallization in Fe-3% Si, Acta Metallurgica et Materialia 38 (10) (1990) 1849–1856. doi:10.1016/0956-7151(90)90296-S.

[14] J. Harase, Coincidence boundary and secondary recrystallization in fcc and bcc metals, Canadian Metallurgical Quarterly 34 (3) (1995) 185–193. doi:10.1016/0008-4433(95)00003-G.

[15] K. Aust, G. Palumbo, Solute effects on the structural and migration behaviour of grain boundaries, Vol. 204-206 of Materials Science Forum, 1996.

[16] I. L. Dillamore, C. J. E. Smith, T. W. Watson, Oriented nucleation in the formation of annealing textures in iron, Metal Science Journal 1 (1) (1967) 49–54.

[17] W. B. Hutchinson, Recrystallisation textures in iron resulting from nucleation at grain boundaries, Acta Metallurgica 37 (4) (1989) 1047–1056.

[18] P. Gangli, J. J. Jonas, T. Urabe, A combined model of oriented nucleation and selective growth for the recrystallization of interstitial-free steels, Metallurgical and Materials Transactions A 26 (9) (1995) 2399–2406.

[19] R. Sebald, G. Gottstein, Modeling of recrystallization textures: interaction of nucleation and growth, Acta Materialia (2002) 12.

[20] I. L. Dillamore, H. Katoh, The mechanisms of recrystallization in cubic metals with particular reference to their orientation-dependence, Metal Science 8 (1) (1974) 73–83.

[21] L. Kestens, J. J. Jonas, Transformation And Recrystallization Textures Associated With Steel Processing, Vol. 14A, ASM International, 2005, pp. 685–700.

[22] W. B. Hutchinson, Development and control of annealing textures in low-carbon steels, International metals reviews 29 (1) (1984) 25–42.

[23] Y. Yoshitomi, K. Iwayama, T. Nagashima, J. Harase, N. Takahashi, Coincidence grain boundary and role of inhibitor for secondary recrystallization in Fe-3% Si alloy, Acta metallurgica et materialia 41 (5) (1993) 1577–1585.

[24] H. J. Grabke, Surface and grain boundary segregation on and in iron and steels, ISIJ International 29 (7) (1989) 529–538. doi:10.2355/isijinternational.29.529.

[25] G. Lyudkovsky, P. K. Rastogi, Effect of Antimony on Recrystallization Behavior and Magnetic Properties of a Nonoriented Silicon Steel, Metallurgical Transactions A 15 (2) (1984) 257–260. doi:10.1007/BF02645109.

[26] I. Tanaka, H. Yashiki, Magnetic properties and recrystallization texture of phosphorus-added non-oriented electrical steel sheets, Journal of Magnetism and Magnetic Materials 304 (2) (2006) 611–613. doi:10.1016/j.jmmm.2006.02.155.

[27] S. Nakashima, K. Takashima, J. Harase, T. Kamijo, Effect of Tin Addition on Primary and Secondary Recrystallizations of Silicon Steel, Materials Transactions, JIM 37 (3) (1996) 462–468. doi:10.2320/matertrans1989.37.462.

[28] S. Suzuki, K. Kuroki, H. Kobayashi, N. Takahashi, Sn Segregation at Grain Boundary and Interface between MnS and Matrix in Fe-3 mass%Si Alloys Doped with Tin, Materials Transactions, JIM 33 (11) (1992) 1068–

1076. doi:10.2320/matertrans1989.33.1068.
[29] M. Godec, M. Jenko, H. J. Grabke, R. Mast, Sn Segregation and Its Influence on Electrical Steel Texture Development, ISIJ International 39 (7) (1999) 742–746. doi:10.2355/isijinternational.39.742.
[30] G. Lyudkovsky, P. K. Rastogi, M. Bala, Nonoriented Electrical Steels, Journal of Metals 38 (1) (1986) 18–26.
[31] N. Mavrikakis, C. Detlefs, P. K. Cook, M. Kutsal, A. Campos, M. Gauvin, P. R. Calvillo, W. Saikaly, R. Hubert, H. F. Poulsen, A. Vaugeois, H. Zapolsky, D. Mangelinck, M. Dumont, C. Yildirim, A multi-scale study of the interaction of Sn solutes with dislocations during static recovery in α-Fe, Acta Materialia 174 (2019) 92–104. doi:10.1016/j.actamat.2019.05.021.
[32] N. Bozzolo, S. Jacomet, R. E. Logé, Fast in-situ annealing stage coupled with EBSD: A suitable tool to observe quick recrystallization mechanisms, Materials Characterization 70 (2012) 28–32. doi:10.1016/j.matchar.2012.04.020.
[33] H. J. Bunge, Texture Analysis in Materials Science, Butterworth-Heinemann, 1969.
[34] N. Mavrikakis, P. R. Calvillo, W. Saikaly, M. Descoins, D. Mangelinck, M. Dumont, Segregation affecting the evolution of primary recrystallization textures in a ternary Fe-Si-Sn alloy, IOP Conf. Ser.: Mater. Sci. Eng. 375 (1) (2018) 012016. doi:10.1088/1757-899X/375/1/012016.
[35] C. M. Sellars, J. A. Whiteman, Recrystallization And Grain Growth In Hot Rolling 13 (3-4) (1978) 187–194.
[36] D. G. Brandon, The structure of high-angle grain boundaries, Acta Metallurgica 14 (11) (1966) 1479–1484. doi:10.1016/0001-6160(66)90168-4.
[37] M. Quadir, B. Duggan, Deformation banding and recrystallization of α fibre components in heavily rolled IF steel, Acta Materialia 52 (13) (2004) 4011–4021. doi:10.1016/j.actamat.2004.05.017.
[38] K. Thompson, D. Lawrence, D. J. Larson, J. D. Olson, T. F. Kelly, B. Gorman, In situ site-specific specimen preparation for atom probe tomography, Ultramicroscopy 107 (2) (2007) 131–139. doi:10.1016/j.ultramic.2006.06.008.
[39] B. Gault, D. Haley, F. de Geuser, M. Moody, E. Marquis, D. Larson, B. Geiser, Advances in the reconstruction of atom probe tomography data, Ultramicroscopy 111 (6) (2011) 448–457. doi:10.1016/j.ultramic.2010.11.016.
[40] M. P. Seah, E. D. Hondros, Grain Boundary Segregation, Proceedings of the Royal Society A: Mathematical, Physical and Engineering Sciences 335 (1601) (1973) 191–212. doi:10.1098/rspa.1973.0121.
[41] B. W. Krakauer, D. N. Seidman, Subnanometer scale study of segregation at grain boundaries in an Fe(Si) alloy, Acta Materialia 46 (17) (1998) 6145–6161. doi:10.1016/S1359-6454(98)00262-6.
[42] N. Mavrikakis, Effect of nano-segregation of tin on recrystallisation and grain growth in automotive steels, PhD thesis, Aix-Marseille University (2018).
[43] K. M. Johnson, W.A., Reaction Kinetics in Processes of Nucleation and Growth. 195 (1939) 416.
[44] P. O. Rossi, C. M. Sellars, Quantitative metallography of recrystallization, Acta materialia 45 (1) (1997) 137–148.
[45] H. Homma, S. Nakamura, N. Yoshinaga, On {h,1,1}, the Recrystallisation Texture of Heavily Cold Rolled BCC Steel, Materials Science Forum 467-470 (2004) 269–274. doi:10.4028/www.scientific.net/MSF.467-470.269.
[46] D. Hull, D. Bacon, Introduction to Dislocations, Elsevier, 2011. doi:10.1016/C2009-0-64358-0.
[47] T. Watanabe, T. Murakami, S. Karashima, Misorientation dependence of grain boundary segregation, Scripta Metallurgica 12 (4) (1978) 361–365.
[48] N. Maruyama, G. D. Smith, 3d Atom Probe Analysis on Nb and Mo Segregation during Recrystallisation of α-Fe, Materials Science Forum 467-470 (2004) 949–956. doi:10.4028/www.scientific.net/MSF.467-470.949.
[49] D. Griffiths, J. N. Riley, Dislocation arrangements in deformed polycrystalline 3% silicon-iron, Acta Metallurgica 14 (6) (1966) 755–773. doi:10.1016/0001-6160(66)90123-4.
[50] T. Nguyen-Minh, J. Sidor, R. Petrov, L. Kestens, Occurrence of shear bands in rotated Goss $\{110\}\langle 110\rangle$ orientations of metals with bcc crystal structure, Scripta Materialia 67 (12) (2012) 935–938. doi:10.1016/j.scriptamat.2012.08.017.
[51] T. Haratani, W. B. Hutchinson, I. L. Dillamore, P. Bate, Contribution Of Shear Banding To Origin Of Goss Texture In Silicon Iron, Met Sci 18 (2) (1984) 57–65.
[52] N. Mavrikakis, W. Saikaly, D. Mangelinck, M. Dumont, Segregation of Sn on migrating interfaces of ferrite recrystallisation: quantification through APT measurements and comparison with the solute drag theory, Materialia 9 (2020) 100541. doi:10.1016/j.mtla.2019.100541.
[53] F. Fournier Dit Chabert, F. Tancret, F. Christien, R. Le Gall, J. Castagné, Finite element simulation of interfacial segregation in dilute alloys, J Mater Sci 42 (2007). doi:10.1007/s10853-007-2001-3.
[54] P. Lejček, P. Šandera, J. Horníková, J. Pokluda, M. Godec, On the segregation behavior of tin and antimony at grain boundariesof polycrystalline bcc iron, Applied Surface Science 363 (2016) 140–144.
[55] A. Inoue, H. Nitta, Y. Iijima, Grain boundary self-diffusion in high purity iron, Acta Materialia 55 (17) (2007) 5910–5916. doi:10.1016/j.actamat.2007.06.041.
[56] D. N. Torres, R. A. Perez, F. Dyment, Diffusion of tin in α-iron, Acta Materialia 48 (11) (2000) 2925–2931. doi:10.1016/S1359-6454(00)00074-4.
[57] L. Klinger, E. Rabkin, Beyond the fisher model of grain boundary diffusion: effect of structural inhomogeneity in the bulk, Acta Materialia 47 (3) (1999) 725–734. doi:10.1016/S1359-6454(98)00420-0.
[58] G. Love, Dislocation pipe diffusion, Acta Metallurgica 12 (6) (1964) 731–737. doi:10.1016/0001-6160(64)90220-2.
[59] M. Legros, G. Dehm, E. Arzt, T. J. Balk, Observation of Giant Diffusivity Along Dislocation Cores, Science 319 (5870) (2008) 1646–1649. doi:10.1126/science.1151771.
[60] O. Ruano, A. Miller, O. Sherby, The influence of pipe diffusion on the creep of fine-grained materials, Materials Science and Engineering 51 (1) (1981) 9–16. doi:10.1016/0025-5416(81)90100-2.
[61] S. V. Divinski, J. Geise, E. Rabkin, C. Herzig, Grain boundary self-diffusion in α-iron of different purity: effect of dislocation enhanced diffusion, Zeitschrift für Metallkunde 95 (10) (2004) 945–952. doi:10.3139/146.018036.
[62] L. Storojeva, D. Ponge, R. Kaspar, D. Raabe, Development of microstructure and texture of medium carbon steel during heavy warm deformation, Acta Materialia 52 (8) (2004) 2209–2220. doi:10.1016/j.actamat.2004.01.024.
[63] P. Bate, B. Hutchinson, A re-evaluation of the mechanism of SIBM, Scripta Materialia 36 (2) (1997) 195–198. doi:10.1016/S1359-6462(96)00361-2.
[64] J. E. Bailey, P. B. Hirsch, The Recrystallization Process in Some Polycrystalline Metals, Proceedings of the Royal Society A: Mathematical, Physical and Engineering Sciences 267 (1328) (1962) 11–30. doi:10.1098/rspa.1962.0080.
[65] M. Theyssier, J. Driver, Recrystallization nucleation mechanism along boundaries in hot deformed Al bicrystals, Materials Science and Engineering: A 272 (1) (1999) 73–82. doi:10.1016/S0921-5093(99)00469-4.
[66] A. Paggi, G. Angella, R. Donnini, Strain induced grain boundary migration effects on grain growth of an austenitic stainless steel during static and metadynamic recrystallization, Materials Characterization 107 (2015) 174–181. doi:10.1016/j.matchar.2015.07.003.
[67] M. Winning, A. Rollett, G. Gottstein, D. Srolovitz, A. Lim, L. Shvindlerman, Mobility of low-angle grain boundaries in pure metals, Philosophical Magazine 90 (22) (2010) 3107–3128. doi:10.1080/14786435.2010.481272.
[68] D. Cram, X. Fang, H. Zurob, Y. Bréchet, C. Hutchinson, The effect of solute on discontinuous dynamic recrystallization, Acta Materialia 60 (18) (2012) 6390–6404. doi:10.1016/j.actamat.2012.08.021.
[69] M. Yasuda, K. Murakami, K. Ushioda, Recrystallization behavior and formation of $\{411\}\langle 148\rangle$ grain from α-fiber grains in heavily cold-rolled fe-3%si alloy, ISIJ International 60 (2020). doi:10.2355/isijinternational.ISIJINT-2020-161.
[70] P. Gobernado, R. Petrov, L. Kestens, Recrystallized $\{311\}\langle 136\rangle$ orientation in ferrite steels, Scripta Materialia 66 (9) (2012) 623–626. doi:10.1016/j.scriptamat.2012.01.056.
[71] P. Gobernado, R. H. Petrov, J. Moerman, C. Barbatti, L. Kestens, Recrystallization Texture of Ferrite Steels: Beyond the γ-Fibre, Materials Science Forum 702-703 (2011) 790–793. doi:10.4028/www.scientific.net/MSF.702-703.790.
[72] H. Takechi, H. Katoh, S. Nagishima, Rolling and annealing textures of

low-carbon steel sheets, Trans AIME 56 (1968) 242.
[73] K. Verbeken, L. Kestens, M. Nave, Re-evaluation of the Ibe-Lücke growth selection experiment in a Fe-Si single crystal, Acta Materialia 53 (9) (2005) 2675–2682. doi:10.1016/j.actamat.2005.02.030.
[74] S. Takajo, C. Merriman, S. Vogel, D. Field, In-situ EBSD study on the cube texture evolution in 3 wt% Si steel complemented by ex-situ EBSD experiment – From nucleation to grain growth, Acta Materialia 166 (2019) 100–112. doi:10.1016/j.actamat.2018.11.054.
[75] B. J. Duggan, W. T. Roberts, Recrystallization Textures in an Iron-1·2% Copper Alloy, Metal Science 9 (1) (1975) 449–454. doi:10.1179/030634575790444711.
[76] Y. Pan, B. L. Adams, On the CSL grain boundary distributions in polycrystals, Scripta Metallurgica et Materialia 30 (8) (1994) 1055–1060. doi:10.1016/0956-716X(94)90554-1.
[77] H. Zurob, Y. Brechet, J. Dunlop, Quantitative criterion for recrystallization nucleation in single-phase alloys: Prediction of critical strains and incubation times, Acta Materialia 54 (15) (2006) 3983–3990. doi:10.1016/j.actamat.2006.04.028.
[78] P. Gangli, L. Kestens, J. J. Jonas, The role of coincident site lattice boundaries during selective growth in interstitial-free steels, Metallurgical and Materials Transactions A 27 (8) (1996) 2178–2186.
[79] L. Kestens, J. J. Jonas, P. Van Houtte, E. Aernoudt, Orientation selective recrystallization of nonoriented electrical steels, Metallurgical and Materials Transactions A 27 (8) (1996) 2347–2358.
[80] J. K. Mackenzie, M. J. Thomson, Some Statistics Associated with the Random Disorientation of Cubes, Biometrika 44 (1/2) (1957) 205. doi:10.2307/2333253.
[81] G. Ibe, K. Lücke, Orientierungszusammenhänge bei der Rekristallisation von Einkristallen einer Eisen-Silizium-Legierung mit 3% Si, Steel research international 39 (9) (1968) 693–703.
[82] M. Sanjari, Y. He, E. J. Hilinski, S. Yue, L. A. Kestens, Development of the $\{113\}\langle uvw\rangle$ texture during the annealing of a skew cold rolled non-oriented electrical steel, Scripta Materialia 124 (2016) 179–183. doi:10.1016/j.scriptamat.2016.07.005.
[83] G.-t. Liu, Z.-q. Liu, P. Yang, W.-m. Mao, Correlation between Primary and Secondary Recrystallization Texture Components in Low-temperature Reheated Grain-oriented Silicon Steel, Journal of Iron and Steel Research, International 23 (11) (2016) 1234–1242. doi:10.1016/S1006-706X(16)30181-9.
[84] R. Suehiro, Y. Hayakawa, T. Takamiya, Effect of sn addition on evolution of primary recrystallization texture in 3% Si steel, ISIJ International 59 (2) (2019) 351–358.